nature biotechnology

Article

https://doi.org/10.1038/s41587-026-03231-z

High numerical aperture confocal volumetric mesoscope reveals mesoscale subcellular dynamics in vivo

Received: 10 November 2025

Accepted: 23 June 2026

Published online: 15 July 2026

Check for updates

Zhi Lu (卢志)[1,2,3,9], Minghuan Wang (汪明欢)[4,9], Wentao Chen (陈文韬)[3,5,9], Manchang Jin (金满昌)[3,5], Laiyu Zhu (朱来余)[2,3], Tianyun Wang (王添运)[3,5], Qi Zhang (张琦)[2,3], Yi Yang (杨懿)[6], Chaowei Zhuang (庄超玮)[6], Jiamin Wu (吴嘉敏)[2,3,7,8] ✉, Wei Wang (王伟)[4] ✉ & Qionghai Dai (戴琼海)[2,3,8] ✉

Simultaneously capturing subcellular dynamics across thousands of cells in mammals remains challenging because of trade-offs among spatial resolution, field of view, imaging speed and sample viability, particularly under high-NA (numerical aperture) conditions. Here we design a high-NA mesoscale objective lens and present a confocal volumetric mesoscope with an NA of 1.05, RUSH3D-HR, achieving ~390-nm resolution across a volume of 2.7 × 2.0 × 0.04 mm^3 at five volumes per second with low phototoxicity. By integrating our previously developed confocal scanning light-field framework with a parallelized deep-learning pipeline, RUSH3D-HR increases experimental efficiency by orders of magnitude. Long-term imaging at 70 billion voxels per second visualizes immune responses such as long-distance collective cell migrations during wound healing and large-scale migrasome generation and neutrophil–macrophage interactions during acute liver failure. Hour-long monitoring over 6,000 neutrophils reveals transient emergent swarming behaviors in mouse spleen during lipopolysaccharide-induced inflammation, which is suppressed with electroacupuncture at ST36, providing direct evidence for the immunomodulatory mechanism of peripheral electrical stimulation.

Millions of cells and organelles in mammals continuously migrate, interact and orchestrate to form sophisticated populational dynamics that drive diverse functionalities in different physiological or pathological states within live mammalian organs[1–5], which are hard to reproduce in vitro[6]. Recent developments of mesoscale intravital fluorescence microscopy[3,7–10] enable the study of large-scale intercellular interactions at single-cell resolution across a mammalian organ in their native states, promoting diverse biological applications[11–13]. However, the progression of many diseases[14–16], especially at the early stage, involves intricate subcellular dynamics in addition to coordinated cellular responses emerging across entire organs[17]. Comprehensive understanding of these transient mesoscale immune dynamics for basic research[18] and drug discovery[19] requires high-fidelity high-throughput volumetric imaging at submicron resolution with millimeter-scale field of view (FOV) and low phototoxicity, which remains a systemic engineering challenge because of the requirement of high numerical aperture (NA)[20,21].

[1]Department of Psychological and Cognitive Sciences, Tsinghua University, Beijing, China. [2]Department of Automation, National Research Center for Information Science and Technology, Tsinghua University, Beijing, China. [3]Institute for Brain and Cognitive Sciences, Tsinghua University, Beijing, China. [4]Department of Neurology, Tongji Hospital, Tongji Medical College, Huazhong University of Science and Technology, Wuhan, China. [5]School of Information Science and Technology, Fudan University, Shanghai, China. [6]Zhejiang Hehu Technology, Hangzhou, China. [7]Beijing Visual Science and Translational Eye Research Institute (BERI), Beijing, China. [8]IDG/McGovern Institute for Brain Research, Tsinghua University, Beijing, China. [9]These authors contributed equally: Zhi Lu, Minghuan Wang, Wentao Chen. ✉e-mail: wujiamin@tsinghua.edu.cn; wwang@vip.126.com; qhdai@tsinghua.edu.cn

NA describes the light collection angle and is a fundamental parameter of a microscope, characterizing the light-gathering ability and spatial resolution set by the diffraction limit. There are three technical challenges restricting the development and application of a high-NA mesoscope to achieve both large FOV and high resolution. Firstly, high-NA imaging systems are more sensitive to optical aberrations originating from either imperfect lens design and fabrication or nonuniform distribution of the refractive index in tissue. Therefore, the FOVs of existing objective lenses with a full NA larger than 1.0 are generally smaller than 1 mm (ref. 22). While adaptive optics can correct optical aberrations, it is usually time consuming and requires complicated systems for multisite correction of spatially nonuniform aberrations[23,24]. Secondly, high NA leads to a shallow depth of field (DOF) and usually requires dense axial scanning to cover a large three-dimensional (3D) volume[2,20], which may also introduce high phototoxicity because of unnecessary excitation of out-of-focus regions in confocal microscopy[11,25]. Single-objective oblique light-sheet techniques[26,27] can achieve fast volumetric imaging with a reduction in phototoxicity; however, they remain incapable of providing millimeter-scale high-NA imaging at millisecond speeds. Lastly, the shallow DOF results in strong contaminations of background fluorescence in scattering tissue, degrading the imaging contrast and fidelity in vivo. Although recent developments in computational imaging shed light on solving these problems individually[3,28–35], addressing them simultaneously to visualize organelle-level subcellular structures across mesoscale FOVs in the native state remains technically unachievable.

Here, we present a confocal volumetric mesoscope with an NA of 1.05, named RUSH3D-HR, achieving subcellular resolution (about 390 nm laterally and 700 nm axially) across a large volume of $2.7 \times 2.0 \times 0.04$ mm^3 at 5 VPS (volumes per second) with low phototoxicity. Unlike prior mesoscale systems that struggle with the high-NA aberration sensitivity, phototoxicity and background contaminations, RUSH3D-HR addresses these challenges through a synergistic integration of three core advances. Firstly, our designed high-NA mesoscale objective lens (named Kunlun) expands the NA to 1.05 over a 2.8-mm FOV to achieve a large lateral space–bandwidth product (SBP; Methods), implemented with wave-optics digital adaptive optics (wDAO)[3,31] to computationally correct aberrations. Compared to existing mesoscale objective lenses of similar NA[22], Kunlun achieves an improvement in lateral SBP of one order of magnitude; furthermore, when compared to objectives with similar lateral SBP[7,36], Kunlun's NA is roughly twofold higher (Fig. 1a). Secondly, we use the scanning light-field framework[29] for parallel high-speed volumetric acquisition while minimizing phototoxicity. Thirdly, our line-confocal scanning light-field strategy[33] provides robust optical sectioning and background rejection across an extended 40-μm axial coverage, effectively overcoming the shallow DOF bottleneck of high-NA optics, to ensure that the full potential of the objective lateral SBP is realized. To manage the huge data throughput (70 billion voxels per second), we developed a fully automated parallelized deep-learning pipeline incorporating denoising[37], multisite aberration correction[31], motion artifact reduction[32] and 3D reconstruction[34]. Diverse applications are demonstrated to show RUSH3D-HR's versatility and robustness. In mouse skin, we tracked collective long-distance cell migrations and morphological diversity during the wound healing process for several hours. In an acute liver failure model induced by acetaminophen (APAP), we observed subcellular neutrophil–macrophage interactions and identified a significant increase in migrasome generation and neutrophil motility, demonstrating efficient discovery of rare immune events in a single trial and greatly reducing the number of animals required for in vivo experiments. By monitoring over 6,000 neutrophils for hours in the mouse spleen during lipopolysaccharide (LPS)-induced inflammation, we discovered transient emergent swarming behaviors of neutrophils randomly distributed across the spleen. With this mesoscale biomarker of inflammation, we validated that electroacupuncture (EA) at ST36 effectively suppressed inflammation, providing direct evidence of peripheral immunomodulation. These results highlight the broad utility of RUSH3D-HR in uncovering mesoscale intercellular emergent dynamics during disease progression, with applications spanning cell biology, immunology and pathology.

Results

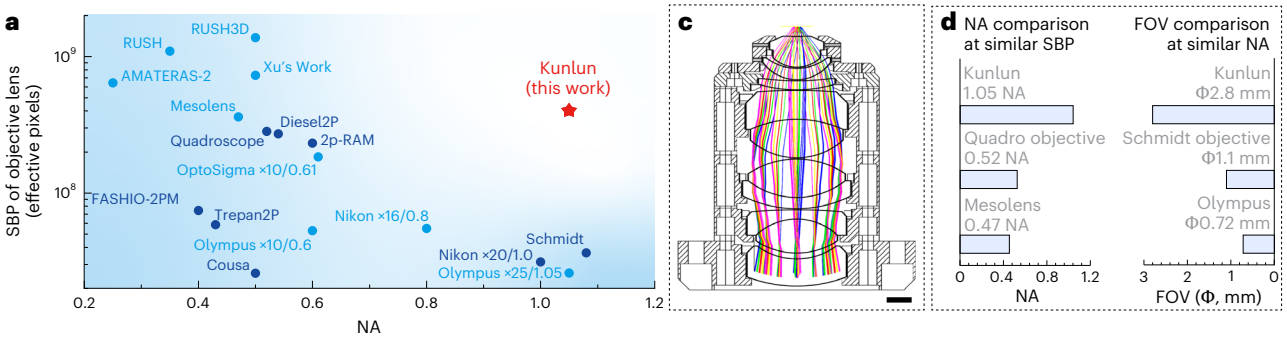
Principle of RUSH3D-HR

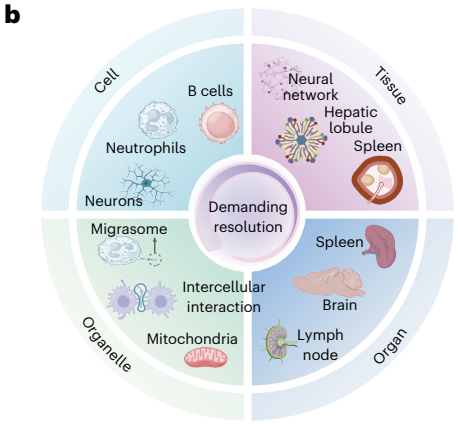
Despite recent advances in mesoscale imaging to observe large-scale cellular dynamics at the organ level[3,9], there remains a gap for subcellular mesoscopes because of the engineering challenge of designing and manufacturing a high-NA wide-FOV objective and the accompanying problems such as background contaminations and shallow DOF (Supplementary Video 1, part I). Therefore, it is generally hard to link microscale organelle behaviors with tissue-level functions of large-scale cells, which is critical for in vivo study of heterogeneous intercellular interactions (Fig. 1b).

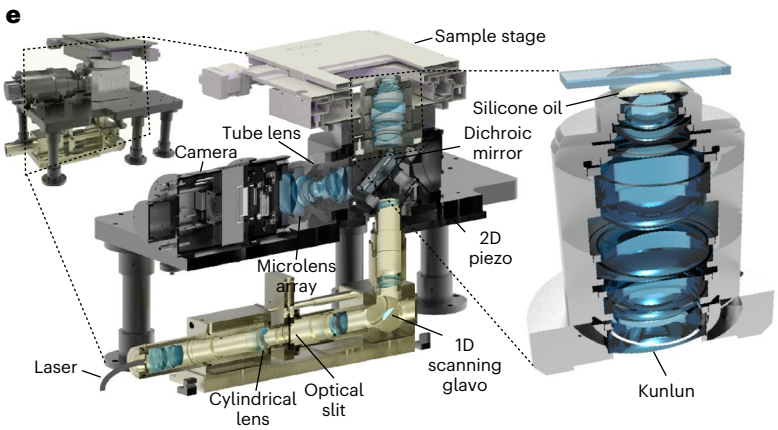
To address this problem, we firstly designed the Kunlun objective lens using a nontelecentric, full-path optical optimization approach[38] (Fig. 1c and Supplementary Fig. 1). Unlike traditional telecentric designs, aberration correction is distributed across both the objective and tube lens, enabling a streamlined ten-element assembly that achieves near-diffraction-limited performance in simulation with uniform aberration distribution across the FOV. The customized Kunlun attains an NA of 1.05 over a vast 2.8-mm-diameter FOV with a large lateral SBP, while maintaining high optical transfer functions (OTFs) and low aberrations across a broad spectral bandwidth from 440 nm to 700 nm and the full imaging range (Supplementary Figs. 2 and 3). The field curvature and geometric distortion are maintained below 2% with the Strehl ratios exceeding 0.8 throughout the imaging plane. Silicone oil (with a refractive index of 1.406) is adopted as the immersion

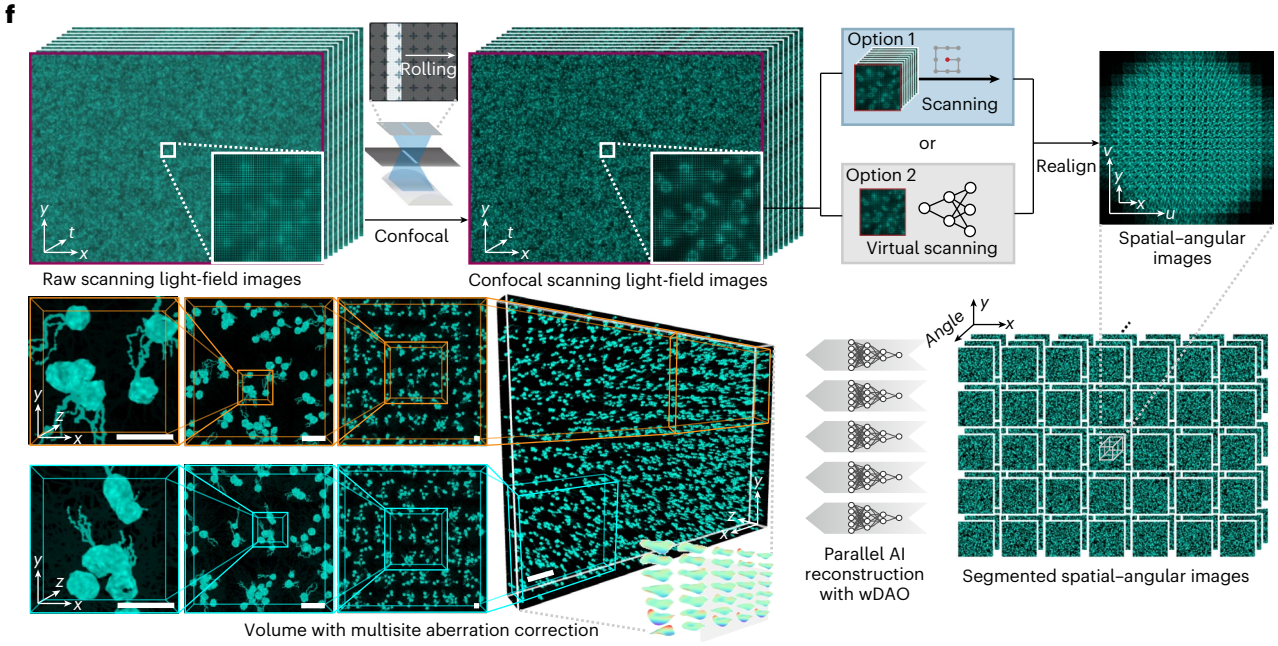
Fig. 1 | Principle of RUSH3D-HR. a, Benchmark of lateral SBP and NA of state-of-the-art mesoscale objective lenses, illustrating the missing gap of high-NA mesoscale systems. The lateral SBPs of objective lenses are calculated theoretically from previous works and the information provided by the manufacturer (Methods). Light-blue dots represent the objectives used with one-photon imaging, while the dark-blue dots represent the objectives designed for multiphoton imaging. **b**, The imaging capability of RUSH3D-HR covering different scales from organelle level to organ level simultaneously. **c**, Optical design of the Kunlun, consisting of ten lens elements to achieve both large lateral SBP and high NA with uniformly low optical aberrations across the FOV. **d**, Comparison of NA and FOV between Kunlun and objectives with similar lateral SBP or NA, including a commercial objective (Olympus XLPLN25XWMP2) and customized objectives (Mesolens, Quadroscope objective and Schmidt objective). **e**, Optical layout of the RUSH3D-HR system, with the Kunlun magnified. **f**, Integration of the Kunlun objective in the confocal scanning light-field imaging framework with a GPU-parallelized data-processing pipeline to obtain high-speed high-resolution mesoscale intravital 3D imaging with multisite aberration correction. Raw measurements after confocal background rejection sequentially undergo motion correction, pixel realignment, segmentation, aberration estimation and 3D reconstruction with multisite aberration correction, all implemented in a GPU-parallelized pipeline for accelerated and robust processing. **g**, Example images with and without motion correction, with comparisons of SSIM shown on the right. In box plots, the center line represents the median, the box limits represent the lower and upper quartiles and the whiskers represent 1.5× the interquartile range ($n = 20$ samples). $P = 1.26 \times 10^{-19}$. Asterisks represent significance levels of comparisons between images without and with motion correction, tested using a two-sided independent t-test. $^*P < 0.05$, $^{**}P < 10^{-2}$, $^{***}P < 10^{-3}$ and $^{****}P < 10^{-4}$. **h**, Comparison of reconstruction speed and image quality across different methods. Scale bars, 10 mm (**c**), 200 μm (original views in **f**), 30 μm (enlarged views in **f**), 5 μm (**g**) and 100 μm (**h**).

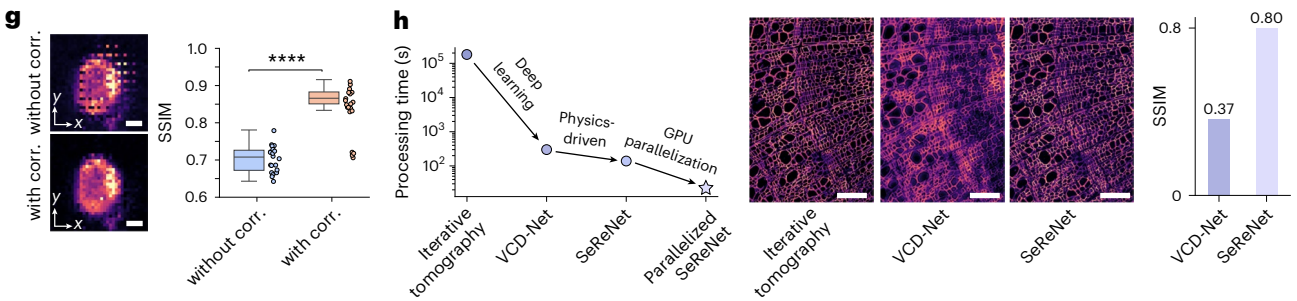
https://doi.org/10.1038/s41587-026-03231-z











https://doi.org/10.1038/s41587-026-03231-z

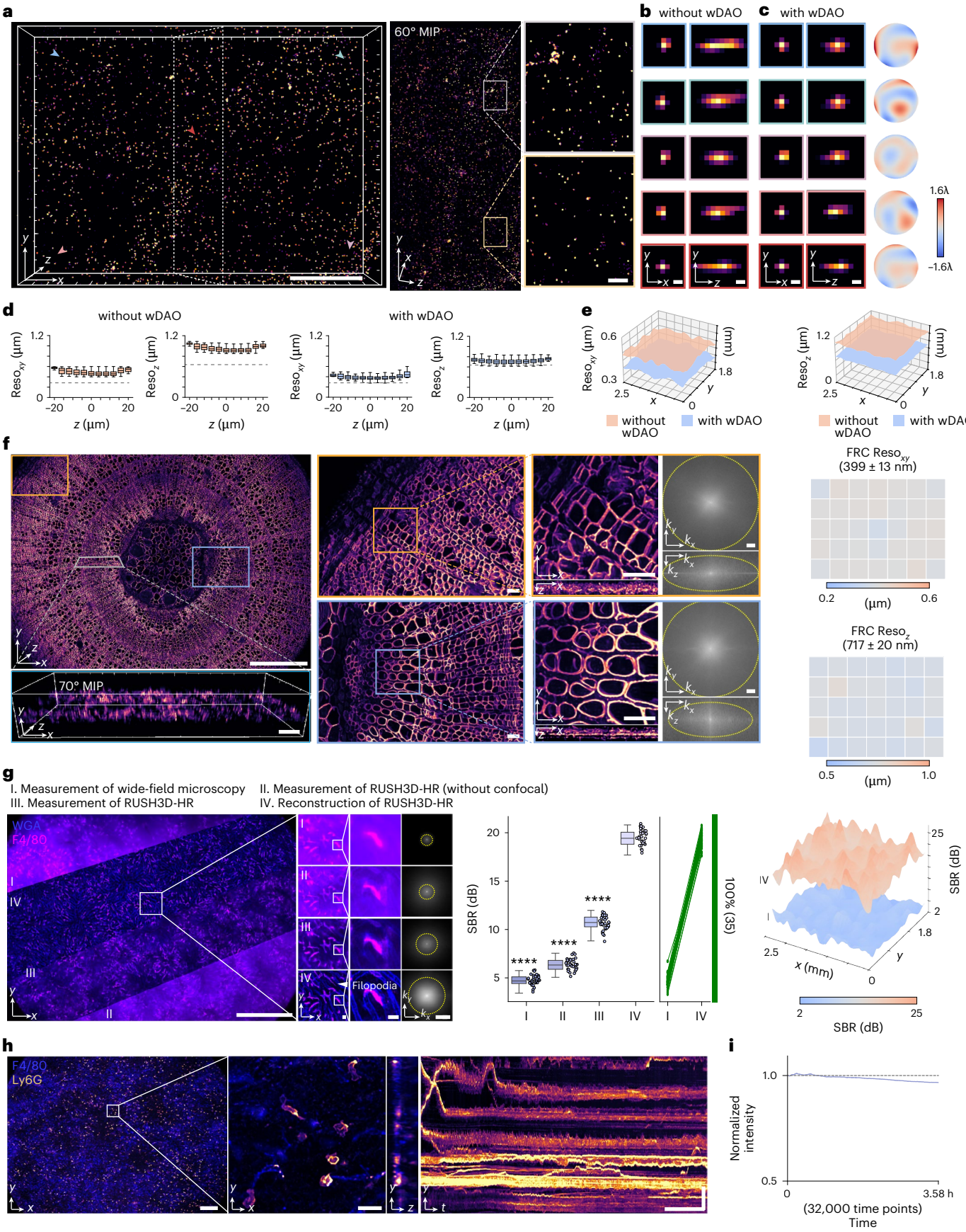


Fig. 2 | Characterization of RUSH3D-HR. a, Two-directional maximum intensity projections (MIPs) of 200-nm-diameter fluorescence beads randomly distributed within a volume of 2.7 × 2.0 × 0.04 mm^3, imaged by RUSH3D-HR. **b**, Orthogonal MIPs of five representative beads from different spatial regions without wDAO. **c**, Left, results after aberration correction using wDAO, showing improved performance. Right, estimated wavefronts. **d**, Box plots of the lateral and axial resolutions of RUSH3D-HR, quantified from FWHMs of Gaussian-fitted bead intensity profiles. Dashed lines indicate the diffraction limit (n = 832 beads for results without wDAO and 1,226 beads for results with wDAO included for statistical analysis). **e**, Heat maps of spatial resolution uniformity across the mesoscale FOV, without and with wDAO. **f**, A 3D rendering and enlarged MIPs of autofluorescent stem tissue slice, acquired by RUSH3D-HR. Fourier transforms of the orthogonal MIPs and resolution maps estimated by FRC over the entire FOV are also shown. **g**, Left, images of macrophages (magenta) and vessels (blue) in a living mouse liver using wide-field microscopy, RUSH3D-HR without and with confocal configuration before 3D reconstruction and RUSH3D-HR after 3D reconstruction. Middle, Fourier transforms of the MIPs and FRC-derived resolution estimates indicated by yellow circles. Right, box plots and heat maps summarize the comparison of SBR for different methods (n = 35 samples). $P = 7.82 \times 10^{-70}$, 1.34×10^{-65} and 1.48×10^{-53}, from left to right. Asterisks represent significance levels of comparisons between each method and RUSH3D-HR after 3D reconstruction, tested using a two-sided independent t-test after Benjamini–Hochberg correction. *$P < 0.05$, **$P < 10^{-2}$, ***$P < 10^{-3}$ and ****$P < 10^{-4}$. **h**, MIPs and kymograph of the neutrophils and vessel in a living mouse liver acquired by RUSH3D-HR, illustrating long-term high-speed imaging continuously over >3 h with more than 30,000 time points. The imaging speed was 2.5 VPS and the laser intensity was kept as low as about 1 mW mm^{-2}. Kymographs were generated by calculating the MIPs along the x and z axes. **i**, Normalized average intensity over time for the dataset in **h**, with the dashed line indicating the value of 1. Scale bars, 500 µm (whole views in **a**,**f**,**g**), 30 µm (enlarged views in **a**,**f**,**g**), 500 nm (**b**), 1 µm^{-1} (Fourier domain in **f**,**g**) and 200 µm spatially in the whole view, 20 µm spatially in the enlarged view and 30 min temporally (**h**). In box plots, the center line represents the median, the box limits represent the lower and upper quartiles and the whiskers represent 1.5× the interquartile range.

medium instead of water to maintain stable long-term imaging and achieve better refractive index matching with biological tissues[39] relative to standard immersion oil (with a refractive index of 1.518). Compared to existing mesoscale objective lenses, we achieve about a twofold improvement in NA and much more uniform imaging performance in the spatial domain[7,22,36] (Fig. 1d and Supplementary Fig. 4).

However, because of the intrinsic aberration sensitivity of high-NA optics, even minute fabrication errors lead to inevitable resolution and SNR degradation and the situation becomes worse for intravital imaging because of the nonuniform distribution of the refractive index in multicellular organisms (Supplementary Fig. 5). To address this spatially nonuniform aberration, we then used the scanning light-field framework to extract high-resolution four-dimensional spatial–angular information, which can record the imaging process up to the diffraction limit for digital manipulation of the light rays in post-processing[29]. This computational imaging framework facilitated the integration of wDAO[3,31] into RUSH3D-HR, enabling accurate estimation and correction of multisite aberrations across a large FOV without reducing the data acquisition speed and thereby tolerating inevitable manufacturing and environmental errors (Supplementary Fig. 6).

While the large NA increases photon efficiency, background contamination also becomes more severe with the shallow DOF, degrading the imaging contrast within living organisms. To overcome this problem, we extended confocal scanning light-field microscopy[33] into the mesoscale realm by implementing a uniform, biaxially elongated line-confocal illumination that is precisely synchronized with camera rolling readout (Supplementary Fig. 7). This configuration uses the rolling shutter as a mobile virtual slit to effectively reject background fluorescence without optical descanning. Therefore, RUSH3D-HR achieves high-speed volumetric imaging with robust optical sectioning across millimeter-scale volumes within a compact platform (Fig. 1e).

Furthermore, mesoscale subcellular imaging inherently generates huge data throughput. The raw spatial–angular data captured by RUSH3D-HR must undergo a multistage computational reconstruction to yield high-resolution 3D volumes. To handle the escalating data scale and complexity, we developed a fully accelerated artificial intelligence (AI)-based processing pipeline specifically tailored for RUSH3D-HR (Fig. 1f and Supplementary Fig. 8). Firstly, raw images were partitioned into 35 sub-FOVs for parallelized processing, where a blockwise correction strategy effectively rectified image distortions and dead pixels to correct nontelecentric distribution of chief rays (Supplementary Fig. 9). Secondly, we developed an automatic algorithm to identify motion artifacts during scanning and implemented the virtual scanning network[32] to correct these artifacts (Fig. 1g and Supplementary Fig. 10). Thirdly, a self-supervised denoising strategy[37] based on the spatial–angular correlation can be used to improve the signal-to-noise ratio (SNR) by about 18 dB in extremely-low-photon conditions (Supplementary Fig. 11). The denoising process is optional depending on different samples. Lastly, to reconstruct the huge data size (about 14,000 × 10,000 × 100 voxels per frame, about 20 GB), conventional processing pipelines[40,41] even with deep learning may take a very long time. We further improved our previously proposed self-supervised learning-based reconstruction network (SeReNet)[34] with multi-GPU parallel processing and multisite wDAO, over 1,000-fold faster than deconvolution algorithms, thereby enabling real-time gigavoxel-scale processing (Fig. 1h and Supplementary Fig. 12).

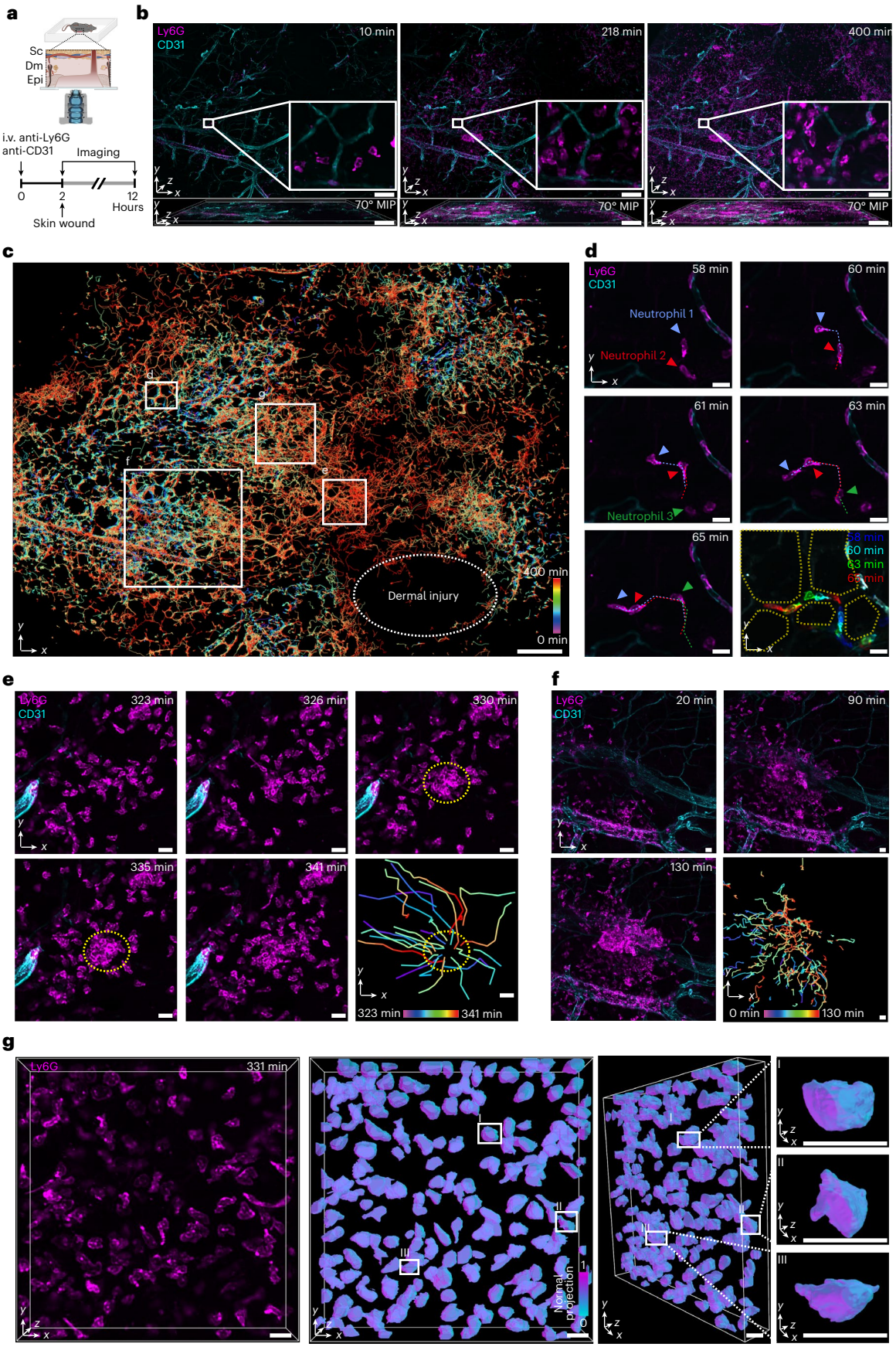
System characterization and benchmark

We then comprehensively evaluated the performance of RUSH3D-HR and benchmarked it against state-of-the-art methods through multiple experimental validations.

Firstly, resolution analyses by fluorescence beads and Fourier ring correlation (FRC) of diverse sample structures confirmed that RUSH3D-HR achieves uniform near-diffraction-limited performance throughout the entire imaging volume. Fluorescent beads with a diameter of 200 nm were randomly embedded in the 3D agar and imaged by RUSH3D-HR. The full widths at half maximum (FWHMs) of the bead intensity profiles along both lateral and axial dimensions demonstrate uniform resolution of 475 ± 53 nm laterally and 930 ± 54 nm axially across the mesoscale FOV (Fig. 2a).

Fig. 3 | Long-term mesoscale tracking of long-distance collective neutrophil migrations during wound healing in mouse dorsal skin. a, Schematic of the epidermal acute imaging window (diameter = 4.0 mm) in mouse dorsal skin, followed by induction of a dermal wound (diameter = 0.8 mm). Epi, epidermis; Dm, dermis; Sc, subcutis. **b**, MIPs and 3D renderings of wounded mouse dorsal skin labeled with neutrophils (magenta) and vessels (cyan) over a volume of 2.7 × 2.0 × 0.04 mm^3 acquired by RUSH3D-HR at three time points. Insets, zoomed-in regions with subcellular resolution. **c**, Overlay of 3D tracked neutrophils trajectories across 400 min (n = 19,992 neutrophils with the traces lasting longer than 10 min), with different colors representing different time points. The dermal wound site is outlined by a white dashed circle. **d**, Time-lapse and color-coded MIPs of the region marked in **c**, illustrating neutrophils migrating around adipose tissue stroma in the dermis and forming an organized migration pattern. Yellow dashed circles mark the boundaries of adipose tissue stroma. Four MIPs at different time points are overlaid together with different colors to better visualize the migration pattern in the bottom-right corner. **e**,**f**, MIPs at different time points and corresponding trajectories of the region marked in **c**, illustrating local neutrophil gathering before reaching the wound site. **g**, Representative local image and automatically extracted cell morphology of neutrophils with zoomed-in views to show clear subcellular structures. Scale bars, 200 µm (**b**,**c**) and 20 µm (**d**–**g**).

https://doi.org/10.1038/s41587-026-03231-z



The degradation of the resolution compared to the diffraction limit results from system aberrations caused by manufacturing errors (Fig. 2b). Aberration correction with wDAO effectively solved this problem and increased the resolution to about 381 ± 42 nm laterally and 707 ± 50 nm axially with an effective axial range of about 40 µm (Fig. 2c,d and Supplementary Fig. 13a–d). Notably, the system maintains isotropic lateral resolution, despite a minor degradation observed when moving away from the native focal plane. With multisite aberration correction, the experimental resolution is uniformly distributed across the entire FOV of 2.7 × 2.0 × 0.04 mm^3 with a small standard deviation of only 48 nm laterally and 95 nm axially (Fig. 2e). This performance was validated against commercial spinning-disk confocal microscopy with a ×30 (1.05 NA) objective lens on static biological tissues, yielding nearly identical results and establishing the reliability of our system (Supplementary Fig. 13e,f). Standardized targets such as the 1951 USAF test chart also confirmed that RUSH3D-HR achieves a spatial resolution of 387.5 nm, clearly visualizing the line pair of element 3 in group 11 with a linewidth of 193.8 nm (Supplementary Fig. 14). We further validated the experimental resolution by measuring FRC on plant stem tissue and neutrophils in mouse spleen. Uniform resolution (399 ± 13 nm laterally and 717 ± 20 nm axially) can be obtained across the entire FOV in vivo with an effective depth range of 40 µm, designed to match the common one-photon scattering penetration depth in mouse liver and spleen (Fig. 2f and Supplementary Fig. 15). These resolution characterizations ensure high-quality uniform imaging performance across the mesoscale FOV at a high imaging frame rate, which is challenging for traditional mesoscopes.

Secondly, we evaluated the signal-to-background ratio (SBR) of RUSH3D-HR with the confocal module, which is critical for high-fidelity imaging in living tissues exhibiting intense background fluorescence. We imaged the superficial layer of a mouse liver with antibody labeling of the neutrophils and vessels in vivo with huge amounts of background fluorescence because of dense labeling. With the confocal scanning light-field framework[33], RUSH3D-HR achieved a high SBR of 19.5 ± 0.8 dB, representing a substantial improvement of about 13 dB compared to its nonconfocal counterpart and about 15 dB relative to traditional wide-field microscopy (Fig. 2g, Supplementary Fig. 16 and Supplementary Video 1, part II). This enhanced optical sectioning enabled clear visualization of fine, subcellular structures such as macrophage filopodia within thick tissues and better image contrast across the entire FOV, thereby ensuring high-fidelity imaging in vivo.

While traditional confocal microscopy can also achieve high-fidelity imaging, there is phototoxicity influencing the native cellular behaviors because of the unnecessary excitation out of the shallow DOF (<0.8 µm). RUSH3D-HR uses the light-field imaging framework to achieve a high-resolution extended DOF of about 40 µm, 50 times larger than traditional confocal microscopy with similar NA, which can solve this problem by keeping the photons focused within axially extended point spread functions (PSFs). We previously validated that the confocal scanning light-field imaging framework could intrinsically reduce the phototoxicity by more than two orders of magnitude compared to conventional confocal microscopy[33]. This advantage persisted at the millimeter-scale FOV in RUSH3D-HR, enabling long-term high-speed mesoscale subcellular imaging of neutrophils labeled using only standard antibodies, which are generally considered prone to rapid photobleaching (Fig. 2h). Both high SNR and clear structural visualization could be achieved with laser intensities as low as ~1 mW mm^{-2}. Notably, there is no clear photobleaching in continuous 3D intravital imaging for over 3 h (>30,000 time points with millisecond-scale volumetric imaging speed), yielding more than 450 trillion voxels (Fig. 2i).

Together, all these characterizations validate that RUSH3D-HR provides high-fidelity confocal mesoscale imaging with a uniform subcellular resolution of about 390 nm laterally and 700 nm axially over the entire FOV of 2.7 × 2.0 × 0.04 mm^3 at 5 VPS, delivering an effective data throughput of 70 billion voxels per second with minimal phototoxicity during prolonged imaging sessions. The performance is generally robust against strong optical aberrations, intense background fluorescence, sample motions and high noise levels.

Monitoring of collective long-distance cell migrations during wound healing

Mesoscale subcellular intravital imaging is essential to observe collective cellular behaviors across a large range in animals such as immune responses and tumor metastasis. During skin wound healing, immune cells migrate directionally toward injury sites to regulate tissue repair in mice, requiring direct tracking of different types of cells within the native tissue microenvironments to understand its collective working mechanisms[42,43]. However, this process involves hours-long, long-distance migration and diverse cell morphological changes that conventional microscopy has struggled to capture in mammals[34]. RUSH3D-HR fills this gap.

To demonstrate its capability, we continuously imaged innate immune responses in the dorsal skin of mice for over 10 h with automatic focus following a minor dermal injury induced by partial epidermal removal (Fig. 3a). Within its millimeter-scale 3D FOV, RUSH3D-HR simultaneously monitored collective cell behaviors at the wound site and surrounding tissues with subcellular details (Fig. 3b). Trajectory analysis of thousands of cells revealed collective long-distance cell migrations toward the wound during healing (Fig. 3c and Supplementary Video 2). Beyond this directed movement, we found that neutrophils navigated through the stromal compartment of dermal adipose tissue, forming net-like migration patterns (Fig. 3d). Notably, some neutrophils halted and gathered before reaching the wound, likely reflecting local sporadic inflammatory responses that recruited small immune clusters (Fig. 3e,f). Subcellular resolution of RUSH3D-HR enabled visualization of diverse cell poses among large neutrophil

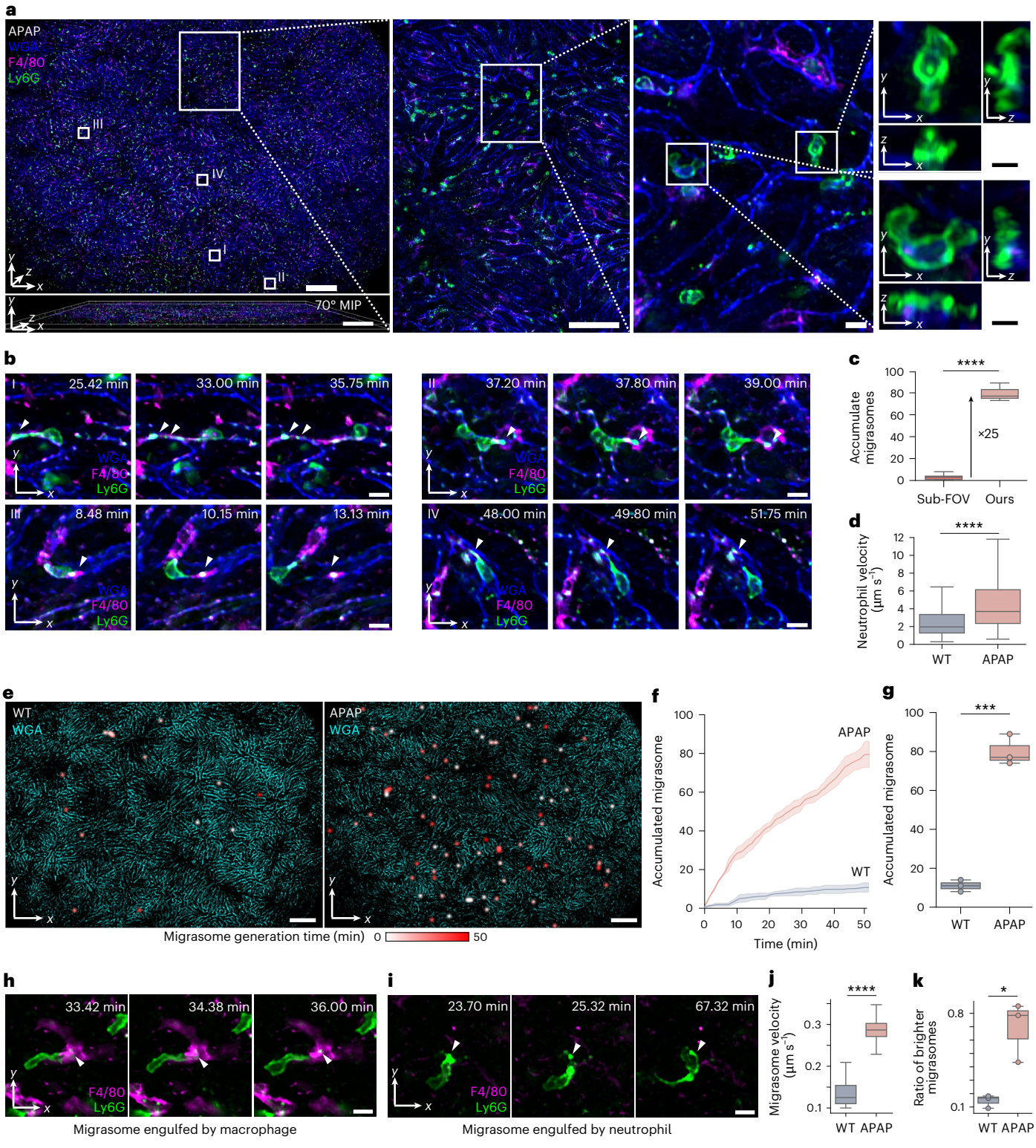
Fig. 4 | Quantitative investigation of migrasome functions during liver failure at the mesoscale. a, MIPs and 3D rendering of an APAP-challenged (300 mg kg^{-1}) mouse liver at $t = 0$ s, spanning a volume of 2.7 × 2.0 × 0.04 mm^3, acquired by RUSH3D-HR at varying zoom levels. Neutrophils (green) and macrophages (magenta) in vessels (blue) are labeled. **b**, Time-lapse MIPs of four representative regions marked in **a**, illustrating the formation of retraction fibers and migrasomes during neutrophil migrations along the vessels. Arrows point to the generated migrasomes. **c**, Box plot exhibiting number of migrasomes generated within sub-FOV (similar to conventional high-NA microscopes) and full FOV ($n = 3$ samples for full FOV, $n = 105$ samples for sub-FOV). $P = 1.43 \times 10^{-65}$. These results indicate that RUSH3D-HR effectively increases the intravital experimental efficiency because of the high throughput. **d**, Box plot exhibiting the average velocity of neutrophils in mice treated with ($n = 8{,}866$) and without APAP ($n = 5{,}765$). $P = 2.97 \times 10^{-247}$. **e**, Color-coded heat map illustrating the spatiotemporal distributions of the migrasome generation events in control and APAP-challenged mice. The intensity of the red color denotes the specific time point for each migrasome generation event overlaid on the MIP of the vessels. **f**, Curves depicting the number of migrasomes accumulated over time with and without APAP. Data are presented as the mean ± s.d. ($n = 3$ mice for each). **g**, Box plot exhibiting the number of migrasome generation events in mice treated with and without APAP ($n = 3$ mice for each). $P = 1.47 \times 10^{-4}$. **h**,**i**, MIPs at different time points showing that a migrasome generated by one neutrophil was engulfed by a macrophage (**h**) or a neutrophil (**i**). **j**, Box plot exhibiting the average velocity of migrasomes in mice treated with and without APAP ($n = 335$ time frames). $P = 1.21 \times 10^{-316}$. **k**, Box plot exhibiting the average ratios of migrasomes that became brighter relative to their previous state over imaging duration in mice treated with and without APAP ($n = 3$ samples). $P = 1.50 \times 10^{-2}$. In box plots, the center line represents the median, the box limits represent the lower and upper quartiles and the whiskers represent 1.5× the interquartile range. Asterisks represent significance levels, tested using a two-sided independent *t*-test. $^*P < 0.05$, $^{**}P < 10^{-2}$, $^{***}P < 10^{-3}$ and $^{****}P < 10^{-4}$. Scale bars, 200 µm (whole views in **a**,**e**), 100 µm (first-level enlarged view in **a**), 10 µm (second-level enlarged view in **a**, enlarged views in **b**,**h**,**i**) and 5 µm (third-level enlarged views in **a**).

https://doi.org/10.1038/s41587-026-03231-z

populations during disease progression. Such fine-grained subcellular information provides critical insights into how distinct cell shapes and pose transitions relate to migratory behaviors and functional states, underscoring the utility of RUSH3D-HR for studying mesoscale collective cell migrations in complex tissue contexts (Fig. 3g).

Investigation of organelle-associated rare patterns in pathological states

The dynamics of cells and organelles within mammalian organisms are highly sophisticated, encompassing common processes such as cell division, interaction and migration, as well as rare but functionally critical events for maintaining microenvironmental homeostasis[44]. For instance, the migrasome[45], a newly discovered organelle that marks the path of migrating cells, has essential roles in developmental system formation[46] and immune surveillance functions[47], especially in pathological states. However, only a small subset of motile cells generate retraction fibers during migration, which may subsequently give rise to migrasomes, making these events inherently sparse. Observing their formation process and dynamic behaviors in vivo is challenging with conventional intravital microscopy, because of the inherent trade-off



between FOV and resolution. Mesoscale subcellular imaging is crucial to capture the spatially extended interactions mediated by migrasomes, as well as to resolve organelle-level dynamics that underpin intercellular communication. Without such capabilities, studies often require dozens of experimental repetitions, posing obstacles for biologists studying the organelle-associated rare pathological patterns.

To demonstrate the capability of RUSH3D-HR in uncovering organelle-associated rare patterns in mesoscale disease environments, we used three-color imaging of RUSH3D-HR to continuously observe neutrophils and macrophages in vessels of living mouse livers at 5 VPS (1.67 VPS for each channel). The mice were challenged with APAP for 4 h before imaging to establish acute liver failure. RUSH3D-HR effectively resolved clear subcellular morphologies across millimeter-scale FOV, corresponding to simultaneous imaging of hundreds of traditional microscopes (Fig. 4a and Supplementary Video 3, part I). Various subcellular rare events, such as large-scale migrasome generation from retraction fibers, which occur randomly within the spatiotemporal domain, became routinely observable during RUSH3D-HR imaging (Fig. 4b). Thus, RUSH3D-HR substantially enhanced the detection efficiency of rare events at the single-trial level, which can greatly reduce the number of animals required for in vivo experiments (Fig. 4c). With these large-scale data, we proceeded to investigate the role of migrasomes in APAP-induced liver failure. Compared to wild-type (WT) mice, APAP-challenged mice exhibited a significantly higher propensity to generate migrasomes with much higher neutrophil motion velocities, potentially as a means to establish immune surveillance (Fig. 4d,e and Supplementary Video 3, part II). Quantitatively, during 50 min of high-speed imaging, there was approximately a sixfold increase in the cumulative number of migrasomes forming in the mouse liver (Fig. 4f,g).

Migrasomes have previously been reported to potentially act as intercellular messengers between immune cells[29]. Using RUSH3D-HR, we captured dynamic interactions between neutrophils and macrophages and discovered that a subset of migrasomes produced by neutrophils could be engulfed either by neutrophils themselves or by macrophages (Fig. 4h,i and Supplementary Video 4, part III). Notably, in APAP-challenged mice, these intercellular communications were substantially enhanced, accompanied by a significant increase in migrasome motility, from 0.13 μm s^{-1} to 0.29 μm s^{-1} (Fig. 4j). Moreover, >70% of migrasomes exhibited visible postformation energy enrichment under APAP challenge, in sharp contrast to <20% observed in controls (Fig. 4k). These observations suggest that, in the context of liver failure, migrasome activity is markedly upregulated, potentially functioning as a pivotal mediator of intercellular communications. By accelerating motility and enhancing postformation energy enrichment, migrasomes may facilitate immune cell coordination, thereby constituting a fundamental mechanism that underlies the orchestration of immune responses under pathological stress.

Transient emergent neutrophil swarming during inflammation in mouse spleens

Early stages of disease progression in living organisms originate from subtle cellular changes within organs, where intricate subcellular dynamics coordinate with large-scale population-level behaviors. In particular, neutrophils can exhibit swarming, a collective, transient aggregation in response to inflammatory cues that amplifies immune efficacy while limiting tissue damage[1,6]. Each swarm represents a coordinated migration of hundreds of neutrophils into a dense cluster before gradually dispersing. Such emergent behaviors are essential for rapid immune responses, yet they have primarily been characterized ex vivo in cultured dishes and could not be observed within the mammalian spleen, where the densely packed and highly dynamic immune microenvironment has remained inaccessible because of technical limitations in FOV, resolution, phototoxicity and optical sectioning.

Using RUSH3D-HR, we were able to directly capture this phenomenon in vivo. In LPS-challenged mouse spleens, imaging was initiated 3 h after injection to capture peak inflammatory responses (Fig. 5a and Supplementary Video 4, part I). Across a 2.8-mm-wide region, RUSH3D-HR revealed coordinated, population-level cell migration, leading to transient emergent swarming behaviors of neutrophils distributed randomly across the whole FOV (Fig. 5b and Supplementary Video 4, part II). Quantitatively, we tracked over 6,000 neutrophils per mouse for 5 h within the inflamed spleens. The number of neutrophils increased by approximately 30% compared to controls (Fig. 5c). Concurrently, their average migration velocity rose from 3.53 μm s^{-1} to 3.80 μm s^{-1} (Fig. 5d). These coordinated changes drove a nearly tenfold rise in swarming frequency, from about two events in controls to about 20 distinct swarms under LPS-induced inflammation (Fig. 5e,f). Such system-level responses that were previously inaccessible by the trade-off between FOV and resolution are clearly resolved by RUSH3D-HR, enabling detailed visualization of dynamic immune patterns of large-scale cells across both spatial and temporal scales throughout the entire organ during LPS-induced inflammation (Fig. 5g,h).

High-resolution imaging further resolved subcellular morphologies, allowing precise tracking of individual neutrophils during swarm formation in densely packed cells, which is challenging for single-cell resolution. RUSH3D-HR revealed that neutrophils progressively migrated toward swarm centers during aggregation, whereas such coordinated migration was absent in controls (Fig. 5i–l and Supplementary Video 4, part III). Moreover, neutrophils in inflamed spleens exhibited elevated velocity, characterized by rapid acceleration during

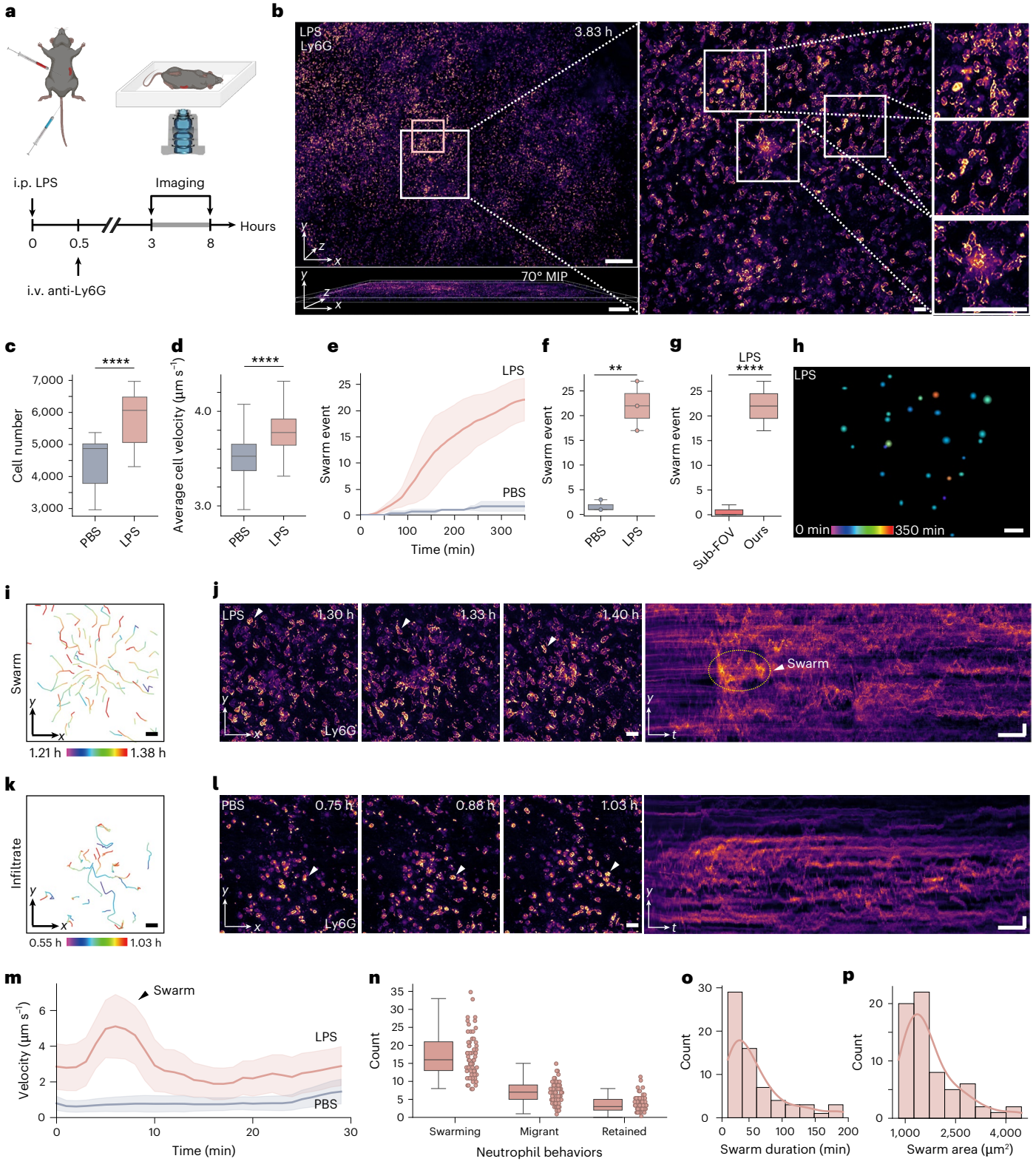
Fig. 5 | Large-scale transient swarming behaviors of neutrophils during inflammation in mouse spleens. a, Schematic of the LPS-induced inflammation model. Mice received an intraperitoneal injection of LPS (5 mg kg^{-1}) for 3 h to induce a proinflammatory phenotype. **b**, 3D renderings of an inflamed spleen labeled with neutrophils at 3 h after LPS challenge across 2.7 × 2.0 × 0.04 mm^3 and imaged with RUSH3D-HR. **c**,**d**, Box plot exhibiting cell number (**c**) and average velocity (**d**) for mice with PBS and LPS (n = 1,050 time frames). $P = 3.83 \times 10^{-316}$ and 7.36×10^{-132}, from left to right (n = 3 mice for each). **e**, Curves of the number of swarming events over time. Data are presented as the mean ± s.d. (n = 3 mice for each). **f**, Box plot exhibiting number of swarming events for mice with PBS and LPS (n = 3 mice for each). $P = 2.36 \times 10^{-3}$. **g**, Box plot exhibiting number of swarming events for sub-FOV (similar to conventional high-NA microscopes) and full FOV (n = 3 samples for full FOV, n = 105 samples for sub-FOV). $P = 3.39 \times 10^{-45}$. **h**, Color-coded heat map illustrating the spatiotemporal distributions of the swarming event in inflamed mice with LPS. The color denotes the time point of appearance for each swarming event. **i**, Overlay of 3D tracked neutrophil trajectories extracted from an enlarged region shown in **b** during swarming in mice with LPS. **j**, Time-lapse MIP images and kymographs illustrating the processes of neutrophil swarming during inflammation corresponding to the same region for **i**. Arrows point to the same cell at different time points. Kymographs were generated by calculating the MIP along the x and z axes, with the dashed yellow circle indicating neutrophil swarming. **k**,**l**, Corresponding results from control mice with an event of infiltrating without swarming. **m**, Curves showing the neutrophil velocities within the local regions (**j**,**l**) over time for controls and inflamed mice. Data are presented as the mean ± s.d. **n**, Box plot exhibiting multiple neutrophil behaviors in cell swarms from inflamed mice. Cells classified as 'swarming' exhibit centripetal migration toward the swarming center, 'migrant' cells move away from the swarming center and 'retained' cells remain stationary (n = 66 represents the number of detected swarming events from three mice). **o**,**p**, Histograms of the temporal duration (**o**) and spatial coverage area (**p**) for the swarming events in inflamed mice with LPS (n = 66 swarming events from three mice. In box plots, the center line represents the median, the box limits represent the lower and upper quartiles and the whiskers represent 1.5× the interquartile range. Asterisks represent significance levels, tested using a two-sided independent t-test. *$P < 0.05$, **$P < 10^{-2}$, ***$P < 10^{-3}$ and ****$P < 10^{-4}$. Scale bars, 200 μm (whole views in **b**,**h**), 20 μm (enlarged views in **b**,**i**–**l**) and 20 μm spatially in the enlarged view and 30 min temporally (kymographs in **j**,**l**).

https://doi.org/10.1038/s41587-026-03231-z

swarm assembly followed by gradual deceleration during dispersal, with peak speeds reaching up to twice the normal velocity (Fig. 5m). Furthermore, we classified neutrophils within local swarm regions into three categories on the basis of their behaviors during the inflammatory response: swarming, migrant and retained. Compared to retained or migrant cells, swarm-associated neutrophils had a significantly larger number (Fig. 5n). Typically, each swarming event lasted approximately 20–180 min and occupied a spatial coverage ranging from roughly 1,000 to 4,000 μm² (Fig. 5o,p). These observations reveal transient neutrophil swarming in the spleen, an unrecognized emergent behavior, highlighting the capability of RUSH3D-HR to uncover a wide range of such transient, collective cellular behaviors that may underlie diverse disease processes.

Validation of inflammation suppression by EA based on the mesoscale biomarker

By capturing the phenomenon of transient neutrophil swarming in inflamed spleens, we next sought to explore its utility as a mesoscale



https://doi.org/10.1038/s41587-026-03231-z

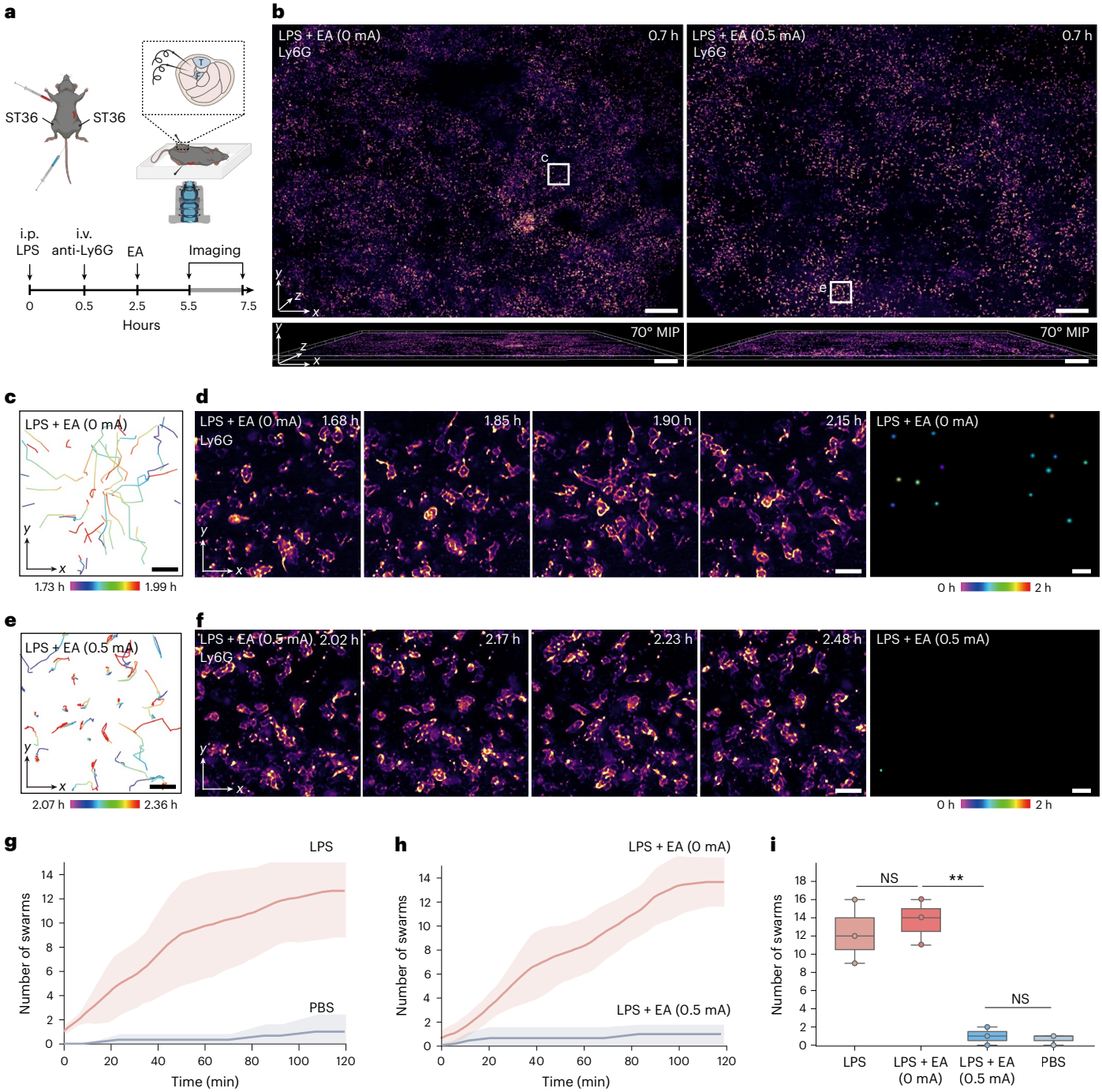


Fig. 6 | EA at ST36 attenuates early-stage inflammation in mouse spleen validated by the mesoscale biomarker. a, Schematic of the experimental paradigm. Mice subjected to LPS-induced inflammation (5 mg kg^{-1}) received EA at the ST36 acupoint 2.5 h after injection. Then, we conducted imaging with RUSH3D-HR after 3 h. **b**, MIPs and 3D renderings of mouse spleens labeled with neutrophils across 2.7 × 2.0 × 0.04 mm^3 obtained by RUSH3D-HR. The mice were LPS-injected with EA treatment of different current intensity to be divided into the LPS-EA (0.5 mA) and LPS-EA (0 mA) groups. Images were acquired at 5.5 h after LPS injection. **c**, Overlay of 3D tracked neutrophil trajectories extracted from an example enlarged region for LPS-EA (0 mA) mice. **d**, Time-lapse MIP images illustrating the process of neutrophil swarming during inflammation (left), with corresponding spatiotemporal distributions of swarming events shown as a color-coded heat map (right). **e**,**f**, Corresponding results from LPS-EA (0.5 mA) mice with an event of infiltrating without swarming. **g**,**h**, Curves of the average number of neutrophil swarming events over time for PBS, LPS, LPS-EA (0 mA) and LPS-EA (0.5 mA) mice. Data are presented as the mean ± s.d. ($n = 3$ mice for each group). **i**, Box plot exhibiting detected swarming events in mice subjected to different treatment conditions. In box plots, the center line represents the median, the box limits represent the lower and upper quartiles and the whiskers represent 1.5× the interquartile range ($n = 3$ mice for each group). $P = 6.21 \times 10^{-1}$, 1.26×10^{-3} and 6.43×10^{-1}, from left to right. Asterisks represent significance levels, tested using a two-sided independent t-test. $^{*}P < 0.05$, $^{**}P < 10^{-2}$, $^{***}P < 10^{-3}$ and $^{****}P < 10^{-4}$. NS, not significant. Scale bars, 200 µm (whole views in **b**, heat maps in **d**,**f**) and 20 µm (enlarged views in **c**–**f**).

biomarker that can be directly visualized in vivo for therapeutic validation. Unlike conventional biomarkers that often rely on endpoint assays or indirect molecular readouts, RUSH3D-HR enables real-time, high-throughput monitoring of mesoscale subcellular activities across spatiotemporal dimensions. The transient and collective nature of neutrophil swarming facilitates early detection of inflammatory states, while subcellular resolvability ensures accurate assessment of immune cell morphology and dynamics.

To demonstrate this utility, we applied RUSH3D-HR to assess the anti-inflammatory efficacy of EA. Previous studies have suggested that EA stimulation at the ST36 (Zusanli) acupoint may modulate physiology at distant sites and exert anti-inflammatory effects in conditions such as sepsis[48,49]. However, the absence of mesoscale high-resolution 3D imaging has limited direct assessment of how EA influences dynamic immune behaviors in vivo. Here, mice with LPS-induced inflammation were treated with EA (0.5 mA) at the ST36 acupoint 2.5 h after LPS administration and RUSH3D-HR imaging was performed 3 h later to evaluate the immune response (Fig. 6a and Methods). By leveraging mesoscale subcellular-resolution 3D imaging during the early stages of disease progression, we found that EA treatment led to a pronounced reduction in neutrophil swarming, indicating effective suppression of LPS-induced inflammation (Fig. 6b and Supplementary Video 5, part I). In localized regions, neutrophils no longer exhibited coordinated aggregation following EA (Fig. 6c–f). As a direct control, we applied acupuncture without electrical stimulation, which did not reduce swarming, and inflammatory activity remained elevated (Supplementary Video 5, part II). Quantitative analysis of neutrophil swarming over time also revealed that the EA-treated mice exhibited a more than fivefold reduction in swarming events, compared to groups with LPS only or LPS-EA without electrical stimulus (0 mA), confirming the anti-inflammatory efficacy of EA at ST36 (Fig. 6g–i). These findings demonstrate that neutrophil swarming can serve as a mesoscale biomarker to directly assess the anti-inflammatory efficacy of peripheral interventions such as EA by tracking thousands of cells with high throughput. This in vivo biomarker responds within hours rather than days and allows direct visualization of collective subcellular dynamics during early disease progression. More broadly, RUSH3D-HR provides a powerful platform for monitoring therapeutic responses and validating treatment effects in vivo and is expected to be applied to a wider range of diseases, such as immune disorders[50], neurological diseases[51] and cardiovascular conditions[52].

Discussion

Disease complexity is largely driven by spatial heterogeneity across tissues and temporal heterogeneity over disease progression. RUSH3D-HR provides a high-fidelity panoramic view in the spatiotemporal domain, addressing the unmet niche of 3D intravital observation of large-scale intercellular interactions at subcellular resolution and millisecond-scale 3D imaging speed in mammals with minimal phototoxicity. Such a capability is enabled by the synergistic design of a high-NA wide-FOV objective lens and the confocal scanning light-field imaging framework in mesoscale, along with an end-to-end fully automated deep-learning processing pipeline to handle massive amounts of data in parallel. With the demonstration of RUSH3D-HR in diverse disease models, including wound healing, liver failure and spleen inflammation, the high-NA confocal volumetric mesoscope not only reveals previously inaccessible mesoscale subcellular behaviors with quantitative characterization of their spatiotemporal dynamics but also increases experimental efficiency by orders of magnitude, thereby greatly improving the reproducibility of intravital studies in biology.

RUSH3D-HR differs from our previously developed RUSH3D[3] by achieving much higher resolution through integrated technical advances and a customized objective lens. Optical design is inherently a process of trade-offs between resolution and FOV. To achieve 3D subcellular resolution (improving from $2.6 \times 2.6 \times 6\ \mu m^3$ to $0.39 \times 0.39 \times 0.7\ \mu m^3$), we engineered the Kunlun objective lens with a high NA of 1.05 and magnification of ×20. This advancement inevitably narrows the FOV from $8 \times 6 \times 0.4\ mm^3$ to $2.7 \times 2.0 \times 0.04\ mm^3$. For constructing the RUSH3D-HR imaging system, we customized a microlens array (MLA), where each individual pitch corresponds to 15×15 camera pixels, ensuring sufficient angular resolution for volumetric reconstruction, coordinated with high-speed scanning through a piezoelectric tilt platform to compensate for potential resolution loss caused by light-field modulation, allowing the system to approach the optical diffraction limit[53] (Methods). Given their distinct spatial scales, RUSH3D-HR serves as a vital complement to RUSH3D for exploring the mesoscale subcellular microenvironment. While RUSH3D focuses on cellular resolution for population-level responses including cortical neuronal activity or germinal center formation, RUSH3D-HR enables the observation of organelle-level dynamics, such as the behavior of migrasomes or mitochondria in inflammatory environments. This capability provides a direct window into how organelle-driven changes in cellular states regulate the microenvironment to uncover fundamental biological mechanisms.

There are still several limitations of RUSH3D-HR at the current stage, which can be addressed in the future by incorporating other techniques. Firstly, there is still a trade-off between snapshot effective axial coverage and resolution. Axial scanning with a large interval can be used for a large axial coverage of over 300 µm to cover dozens of layers of cells in cleared tissues at high speed (Supplementary Fig. 17). Wavefront coding methods can also be integrated to increase the effective depth range[54]. Secondly, the penetration depth is fundamentally limited by the tissue scattering and the one-photon excitation, especially in scenarios involving deeper imaging or highly scattering samples. Future improvements including the use of near-infrared fluorescence labeling techniques[55] or the imaging framework of two-photon light-field excitation[30] hold the potential to extend RUSH3D-HR's capabilities to substantially deeper tissue layers. Thirdly, structured illumination approaches[56,57] can be further incorporated into the current imaging system to achieve super-resolution mesoscale intravital imaging with better resolution for the detailed structures of organelles such as mitochondria and the endoplasmic reticulum during disease progression. Lastly, fluorescence labeling is required for molecular specificity, with only four spectral channels currently available for multiplexed imaging. Hyperspectral imaging or other imaging dimensions such as fluorescence lifetime can be used for simultaneous observation of more channels. In addition, conducting spatial transcriptomics[58,59] analysis after functional imaging of RUSH3D-HR can provide additional molecular information to couple functional cellular behaviors, thereby delivering a more comprehensive landscape of mesoscale microenvironments during diverse physiological and pathological states.

Nevertheless, RUSH3D-HR provides a subcellular mesoscale imaging platform to link microscale subcellular dynamics within each single cell and macroscale organ-level functions for the study of intercellular interactions in vivo.

Online content

Any methods, additional references, Nature Portfolio reporting summaries, source data, extended data, supplementary information, acknowledgements, peer review information; details of author contributions and competing interests; and statements of data and code availability are available at https://doi.org/10.1038/s41587-026-03231-z.

References

1. Kienle, K. et al. Neutrophils self-limit swarming to contain bacterial growth in vivo. *Science* **372**, eabe7729 (2021).
2. Liu, T.-L. et al. Observing the cell in its native state: Imaging subcellular dynamics in multicellular organisms. *Science* **360**, eaaq1392 (2018).

3. Zhang, Y. et al. Long-term mesoscale imaging of 3D intercellular dynamics across a mammalian organ. *Cell* **187**, 6104–6122 (2024).
4. Stoll, S., Delon, J., Brotz, T. M. & Germain, R. N. Dynamic imaging of T cell–dendritic cell interactions in lymph nodes. *Science* **296**, 1873–1876 (2002).
5. Qi, H., Cannons, J. L., Klauschen, F., Schwartzberg, P. L. & Germain, R. N. SAP-controlled T–B cell interactions underlie germinal centre formation. *Nature* **455**, 764–769 (2008).
6. Strickland, E. et al. Self-extinguishing relay waves enable homeostatic control of human neutrophil swarming. *Dev. Cell* **59**, 2659–2671 (2024).
7. McConnell, G. et al. A novel optical microscope for imaging large embryos and tissue volumes with sub-cellular resolution throughout. *Elife* **5**, e18659 (2016).
8. Sofroniew, N. J., Flickinger, D., King, J. & Svoboda, K. A large field of view two-photon mesoscope with subcellular resolution for in vivo imaging. *Elife* **5**, e14472 (2016).
9. Fan, J. et al. Video-rate imaging of biological dynamics at centimetre scale and micrometre resolution. *Nat. Photonics* **13**, 809–816 (2019).
10. Kim, T. H. & Schnitzer, M. J. Fluorescence imaging of large-scale neural ensemble dynamics. *Cell* **185**, 9–41 (2022).
11. Wu, Y. et al. Multiview confocal super-resolution microscopy. *Nature* **600**, 279–284 (2021).
12. Pittet, M. J. & Weissleder, R. Intravital imaging. *Cell* **147**, 983–991 (2011).
13. Hor, J. L. & Germain, R. N. Intravital and high-content multiplex imaging of the immune system. *Trends Cell Biol.* **32**, 406–420 (2022).
14. Shi, Q. et al. Cross-tissue multicellular coordination and its rewiring in cancer. *Nature* **643**, 529–538 (2025).
15. Jones, D. L. et al. An injury-induced mesenchymal-epithelial cell niche coordinates regenerative responses in the lung. *Science* **386**, eado5561 (2024).
16. Zeng, Q. et al. Spleen fibroblastic reticular cell-derived acetylcholine promotes lipid metabolism to drive autoreactive B cell responses. *Cell Metab.* **35**, 837–854 (2023).
17. Crainiciuc, G. et al. Behavioural immune landscapes of inflammation. *Nature* **601**, 415–421 (2022).
18. Germain, R. N., Robey, E. A. & Cahalan, M. D. A decade of imaging cellular motility and interaction dynamics in the immune system. *Science* **336**, 1676–1681 (2012).
19. Conway, J. R. W., Carragher, N. O. & Timpson, P. Developments in preclinical cancer imaging: innovating the discovery of therapeutics. *Nat. Rev. Cancer* **14**, 314–328 (2014).
20. Chen, B. C. et al. Lattice light-sheet microscopy: imaging molecules to embryos at high spatiotemporal resolution. *Science* **346**, 1257998 (2014).
21. Lu, R. et al. Rapid mesoscale volumetric imaging of neural activity with synaptic resolution. *Nat. Methods* **17**, 291–294 (2020).
22. Voigt, F. F. et al. Reflective multi-immersion microscope objectives inspired by the Schmidt telescope. *Nat. Biotechnol.* **42**, 65–71 (2024).
23. Hampson, K. M. et al. Adaptive optics for high-resolution imaging. *Nat. Rev. Methods Prim.* **1**, 68 (2021).
24. Ji, N. Adaptive optical fluorescence microscopy. *Nat. Methods* **14**, 374–380 (2017).
25. Minsky, M. Memoir on inventing the confocal scanning microscope. *Scanning* **10**, 128–138 (1988).
26. Voleti, V. et al. Real-time volumetric microscopy of in vivo dynamics and large-scale samples with SCAPE 2.0. *Nat. Methods* **16**, 1054–1062 (2019).
27. Yang, B. et al. DaXi—high-resolution, large imaging volume and multi-view single-objective light-sheet microscopy. *Nat. Methods* **19**, 461–469 (2022).
28. Prevedel, R. et al. Simultaneous whole-animal 3D imaging of neuronal activity using light-field microscopy. *Nat. Methods* **11**, 727–730 (2014).
29. Wu, J. et al. Iterative tomography with digital adaptive optics permits hour-long intravital observation of 3D subcellular dynamics at millisecond scale. *Cell* **184**, 3318–3332 (2021).
30. Zhao, Z. et al. Two-photon synthetic aperture microscopy for minimally invasive fast 3D imaging of native subcellular behaviors in deep tissue. *Cell* **186**, 2475–2491 (2023).
31. Wu, J. et al. An integrated imaging sensor for aberration-corrected 3D photography. *Nature* **612**, 62–71 (2022).
32. Lu, Z. et al. Virtual-scanning light-field microscopy for robust snapshot high-resolution volumetric imaging. *Nat. Methods* **20**, 735–746 (2023).
33. Lu, Z. et al. Long-term intravital subcellular imaging with confocal scanning light-field microscopy. *Nat. Biotechnol.* **43**, 569–580 (2025).
34. Lu, Z. et al. Physics-driven self-supervised learning for fast high-resolution robust 3D reconstruction of light-field microscopy. *Nat. Methods* **22**, 1545–1555 (2025).
35. Brady, D. J. et al. Multiscale gigapixel photography. *Nature* **486**, 386–389 (2012).
36. Clough, M. et al. Flexible simultaneous mesoscale two-photon imaging of neural activity at high speeds. *Nat. Commun.* **12**, 6638 (2021).
37. Lu, Z. et al. Leveraging spatial-angular redundancy for self-supervised denoising of 3D fluorescence imaging without temporal dependency. *Nat. Commun.* **16**, 11608 (2025).
38. Xu, X. et al. Large-field objective lens for multi-wavelength microscopy at mesoscale and submicron resolution. *Opto-Electron. Adv.* **7**, 230211–230212 (2024).
39. Bolin, F. P., Preuss, L. E., Taylor, R. C. & Ference, R. J. Refractive index of some mammalian tissues using a fiber optic cladding method. *Appl. Opt.* **28**, 2297–2303 (1989).
40. Lu, Z. et al. Phase-space deconvolution for light field microscopy. *Opt. Express* **27**, 18131 (2019).
41. Wang, Z. et al. Real-time volumetric reconstruction of biological dynamics with light-field microscopy and deep learning. *Nat. Methods* **18**, 551–556 (2021).
42. Lämmermann, T. et al. Neutrophil swarms require LTB4 and integrins at sites of cell death in vivo. *Nature* **498**, 371–375 (2013).
43. Ng, L. G. et al. Visualizing the neutrophil response to sterile tissue injury in mouse dermis reveals a three-phase cascade of events. *J. Invest. Dermatol.* **131**, 2058–2068 (2011).
44. Chen, S. et al. Myeloid MAS-driven macrophage efferocytosis promotes resolution in ischemia-stressed mouse and human livers. *Sci. Transl. Med.* **17**, eadr2725 (2025).
45. Ma, L. et al. Discovery of the migrasome, an organelle mediating release of cytoplasmic contents during cell migration. *Cell Res.* **25**, 24–38 (2015).
46. Jiang, D. et al. Migrasomes provide regional cues for organ morphogenesis during zebrafish gastrulation. *Nat. Cell Biol.* **21**, 966–977 (2019).
47. Jiang, D. et al. Neutrophil-derived migrasomes are an essential part of the coagulation system. *Nat. Cell Biol.* **26**, 1110–1123 (2024).
48. Liu, S. et al. Somatotopic organization and intensity dependence in driving distinct NPY-expressing sympathetic pathways by electroacupuncture. *Neuron* **108**, 436–450 (2020).
49. Liu, S. et al. A neuroanatomical basis for electroacupuncture to drive the vagal–adrenal axis. *Nature* **598**, 641–645 (2021).
50. Pisetsky, D. S. Pathogenesis of autoimmune disease. *Nat. Rev. Nephrol.* **19**, 509–524 (2023).
51. Huang, T. et al. Identifying the pathways required for coping behaviours associated with sustained pain. *Nature* **565**, 86–90 (2019).
52. Tzahor, E. & Dimmeler, S. A coalition to heal—the impact of the cardiac microenvironment. *Science* **377**, eabm4443 (2022).

53. Lu, Z. et al. A practical guide to scanning light-field microscopy with digital adaptive optics. *Nat. Protoc.* **17**, 1953–1979 (2022).
54. Zhang, Y. et al. Multi-focus light-field microscopy for high-speed large-volume imaging. *PhotoniX* **3**, 30 (2022).
55. Wang, F. et al. In vivo non-invasive confocal fluorescence imaging beyond 1,700 nm using superconducting nanowire single-photon detectors. *Nat. Nanotechnol.* **17**, 653–660 (2022).
56. Kner, P., Chhun, B. B., Griffis, E. R., Winoto, L. & Gustafsson, M. G. L. Super-resolution video microscopy of live cells by structured illumination. *Nat. Methods* **6**, 339–342 (2009).
57. Li, D. et al. Extended-resolution structured illumination imaging of endocytic and cytoskeletal dynamics. *Science* **349**, aab3500 (2015).
58. Ståhl, P. L. et al. Visualization and analysis of gene expression in tissue sections by spatial transcriptomics. *Science* **353**, 78–82 (2016).
59. Chen, A. et al. Spatiotemporal transcriptomic atlas of mouse organogenesis using DNA nanoball-patterned arrays. *Cell* **185**, 1777–1792 (2022).

Publisher's note Springer Nature remains neutral with regard to jurisdictional claims in published maps and institutional affiliations.

Open Access This article is licensed under a Creative Commons Attribution 4.0 International License, which permits use, sharing, adaptation, distribution and reproduction in any medium or format, as long as you give appropriate credit to the original author(s) and the source, provide a link to the Creative Commons licence, and indicate if changes were made. The images or other third party material in this article are included in the article's Creative Commons licence, unless indicated otherwise in a credit line to the material. If material is not included in the article's Creative Commons licence and your intended use is not permitted by statutory regulation or exceeds the permitted use, you will need to obtain permission directly from the copyright holder. To view a copy of this licence, visit http://creativecommons.org/licenses/by/4.0/.

© The Author(s) 2026

Methods

Experimental setup

The Kunlun was designed in a nontelecentric configuration, forming an imaging system in conjunction with the tube lens. The full optical assembly consists of 17 lenses, with a distance of over 90 mm between the objective and tube lens, providing sufficient space for the placement of a dichroic mirror. The surface of the objective lens in contact with the sample was designed to be flat for ease of silicone oil immersion. The optical and mechanical components were fabricated by Hangzhou Zhida Optics.

In the construction of the RUSH3D-HR system, a multichannel laser source (LDI-primer-488, 89 North) was used for illumination, which has a built-in 'despeckler' function to avoid illumination speckles within the sample. The core of the confocal scanning light-field framework involves restricting the illumination beam to a light sheet and precisely synchronizing it with the camera rolling shutter of equivalent width. This mechanism achieves volumetric confocal imaging while effectively rejecting out-of-focus light beyond the 40-μm DOF. To achieve volumetric excitation, the linewidth of the light sheet along the *y* axis in our system is not minimized; instead, it is designed to be much larger than the optical diffraction limit. To implement this principle, the laser was passed through a cylindrical lens (focal length: 38 mm; LJ1765L1-A, Thorlabs), an optical slit (length: 5 mm, width: 200 μm) and several relay lenses before entering the objective lens, which project biaxially elongated line-confocal illumination onto the sample. The linewidth is approximately 16 μm along the *y* axis (Supplementary Fig. 7). Because of the low NA of the illumination beam, the variation in thickness across the 40-μm effective axial (*z* axis) range is negligible, ensuring consistent performance for 3D volumetric imaging. A one-dimensional (1D) galvanometer mirror was inserted into the illumination path to scan the light, covering the full FOV. On the detection path, the emitted fluorescence was reflected by a multiband dichroic mirror (ZT405/488/555/640, 50 × 70 × 5 mm; Chroma) and into a custom-built tube lens, before being captured by a high-resolution camera (QHY411, QHYCCD, pixel size of 3.76 μm). A customized MLA (square grid, pitch size of 56.4 μm, corresponding to 15 × 15 pixels, focal length: 536.4 μm, F-number: 9.5) was mounted on the sensor surface to achieve light-field modulation. To maintain a compact system, a two-dimensional (2D) piezoelectric tilt platform (P54.T0S, Core Morrow) was used to adjust the angle of the dichroic mirror, enhancing the spatial sampling rate. A 3D motorized stage (H117P1XD, PS3H122R, Prior Scientific) controlled the lateral and axial positioning of the sample holders. Customized control boards (BK-16-1005, Zhongke Zhenghong) were used to synchronize the camera, lasers, 2D tilt platform and 1D galvanometer for precise imaging operations. Detailed imaging conditions and parameters used in biological experiments, including fluorescent label, laser, excitation power, exposure time and volumetric imaging rate, are illustrated in Supplementary Table 1.

Full-path optical optimization approach for Kunlun

Firstly, on the basis of the design requirements of NA of 1.05, magnification of ×20, large FOV and broad spectral bandwidth, we established an initial structure in Zemax OpticStudio software (version 19.4). To alleviate the design constraints on the objective lens, a finite conjugate configuration was adopted. The optical power was initially distributed between the objective and the tube lens, with lens curvatures and air gaps adjusted to ensure beam clearance and convergence at the image plane.

Secondly, the objective lens was primarily optimized to correct spherical aberration, coma and chromatic aberration. In the early stages, a default merit function targeting the root-mean-square (r.m.s.) spot radius was used. By selecting appropriate glass materials and refining the radii of curvature, center thicknesses and air gaps, we systematically reduced the systemic chromatic and spherical aberrations, while the tube lens was used to balance the residual spherical aberration.

Thirdly, once the primary aberrations were suppressed, the merit function was switched to minimize the optical path difference. We further controlled field curvature and geometric distortion by adjusting the curvature, spacing and materials of the rear lens groups within the tube lens assembly.

Fourthly, during the fine-tuning phase, we focused on enhancing the OTF. Specific operands were added to the merit function to drive the OTF toward the diffraction limit across the entire FOV.

Fifthly, we performed a manufacturability analysis for each element, incorporating constraints such as edge thickness and centering coefficients. A comprehensive tolerance analysis and sensitivity assessment were conducted using Monte Carlo simulations.

For highly sensitive elements, we returned to the earlier optimization stages to redistribute optical power or adjust radii of curvature to improve stability. This iterative process yielded the final full-path optical optimization.

AI-based automated processing pipeline

To fully leverage the advantages of RUSH3D-HR, an engineering-oriented integration was performed to enhance automation, robustness and efficiency, with the development of an AI-based processing pipeline. This pipeline is illustrated in detail in Fig. 1f and Supplementary Fig. 8. The individual components of the pipeline are described in detail.

Autofocusing and levelling. Before data acquisition, the offset between two angular images in preview can be determined by calculating the spatial–angular correlation. When the sample is in focus, the overall image offset should be zero. A feedback mechanism is used to control the motorized stage, enabling autofocusing by raising or lowering the sample. Simultaneously, when the sample plane is not perpendicular to the optical axis, the offset along the 35 sub-FOVs will differ. Another feedback mechanism adjusts the three angular degrees of freedom of the motorized stage to achieve automatic levelling.

Image acquisition and partition. The acquisition process of camera is synchronized with the multichannel lasers, 1D galvanometer mirror and 2D piezoelectric tilt platform. Each captured image is automatically segmented into 35 sub-FOVs for storage. Each sub-FOV contains 161 × 161 pixels and adjacent sub-FOVs overlap by 30 × 30 pixels to facilitate subsequent image stitching. The image acquisition speed can reach up to 6 fps.

Distortion correction. Because of inaccuracies in the MLA fabrication or nontelecentric optical paths, spatially nonuniform distortion may occur in the raw light-field images. The distortion can be modeled with parameters and corrected through inverse mapping. The distortion parameters have two components, the intrinsic parameter matrix K, which defines the internal characteristics, and the distortion coefficients $(k_1, k_2, k_3, p_1, p_2)$, which model radial and tangential distortions. The intrinsic parameters matrix K is given by $K = \begin{bmatrix} f_x & 0 & c_x \\ 0 & f_y & c_y \\ 0 & 0 & 1 \end{bmatrix}$, where f_x and f_y are the focal lengths and (c_x, c_y) is the principal point. Given a normalized pixel coordinate $(x, y, 1)^{\mathrm{T}}$ on raw light-field images, the intrinsic-parameter-corrected coordinate (u, v) is obtained by $\begin{bmatrix} u \\ v \\ 1 \end{bmatrix} = K \begin{bmatrix} x \\ y \\ 1 \end{bmatrix}$. Then, the final undistorted coordinate (x_d, y_d) is computed by using distortion coefficients as

$$r^2 = u^2 + v^2$$

$$x_d = u(1 + k_1 r^2 + k_2 r^4 + k_3 r^6) + 2p_1 uv + p_2(r^2 + 2u^2)$$

$$y_d = v(1 + k_1 r^2 + k_2 r^4 + k_3 r^6) + p_1(r^2 + 2v^2) + 2p_2 uv$$

By manually annotating 12 coordinates at different positions across the entire FOV, the distortion parameters can be fitted with the

least-squares method. Lastly, all the mappings from raw image coordinates to undistorted coordinates are calculated and segmented into 35 sub-FOV undistorted maps for parallel processing. The detailed pipeline for distortion correction is illustrated in Supplementary Fig. 9a. This process is system dependent and only needs to be calibrated once after constructing the system.

Pixel realignment. In a light-field setup, each pixel behind a microlens corresponds to a specific angle[53]. Different microlenses represent different spatial sampling points. Through pixel realignment, light-field images can be transformed into spatial–angular images. In RUSH3D-HR, a 3 × 3 scanning mode is used to increase the spatial sampling rate, where the image shift distance is one third the size of each microlens. Spatial–angular images from nine scanning positions can be combined to form a high-resolution spatial–angular image.

White balance. Because of nonuniform transmittance caused by the MLA defects or contamination, spatial–angular images may contain dead pixels that hinder the clear visualization of structures. To address this, a white balance operator is applied, as detailed in Supplementary Fig. 9b. A fluorescence plate is imaged and normalized to generate a standard matrix, which is then used to divide the captured biological images, removing dead pixels. This process is system dependent and only needs to be calibrated once after constructing the system.

Motion correction. When the sample moves rapidly, noticeable changes occur across nine consecutive scanning light-field images, leading to motion artifacts in the spatial–angular images. To address this, we previously developed a virtual scanning network[32] for motion artifact removal through deep learning. The virtual scanning network is a physics-based deep-learning framework that increases the spatial sampling rate of unscanned light-field measurements by exploring the frequency aliasing between different angles with broad generalization capability. However, this process relied on manually determining whether motion correction was necessary. To address this, we incorporated an automated module into the pipeline, as detailed in Supplementary Fig. 10. Because of the 3 × 3 scanning mode used in RUSH3D-HR, we introduced a Laplacian kernel[60] $K_m = \begin{pmatrix} k_m & k_m & k_m \\ k_m & k_m & k_m \\ k_m & k_m & k_m \end{pmatrix}$, where $k_m = \begin{pmatrix} -1/8 & -1/8 & -1/8 \\ -1/8 & 1 & -1/8 \\ -1/8 & -1/8 & -1/8 \end{pmatrix}$, capable of effectively extracting regions with motion artifacts. The grayscale values in these
regions are then transformed nonlinearly to create a weight map that reflects the motion level. A larger artifact results in a greater weight. To preserve the regions without motions as much as possible, the raw spatial–angular images and the results from the virtual scanning network are combined on the basis of the weight map. Typically, motion artifacts arising from local cellular dynamics are effectively and precisely rectified by our processing framework. Because the time interval for a single light-field acquisition is sufficiently short, the biological sample can be considered quasistatic during each individual capture. This ultrashort exposure time ensures that the sample is effectively fixed within each frame. Only a few subsets of moving cells exhibiting detectable artifacts require correction by the pipeline. Furthermore, for global movement of the tissue potentially induced by respiration, which manifests as consistent motion artifacts across all 35 sub-FOVs, the Laplacian kernel can also detect the presence of motion artifacts at every individual pixel, ensuring that the entire FOV is systematically processed and rectified by the virtual scanning network. We can also apply the exact same processing pipeline across all 35 sub-FOVs to ensure globally uniform correction. Consequently, global motion can be effectively rectified. The code for the virtual scanning network can be obtained from GitHub (https://github.com/THU-IBCS/VsLFM-master). During network training, we used simulated beads, bubbles, tubes and scanning volumes of sliced samples as the dataset and trained for 40 epochs, taking 1.5 h on an NVIDIA A100 GPU. It should be noted that this motion correction method is theoretically superior to TW-Net[34], which is a more complex approach relying on prior self-supervised training to detect motion artifacts, followed by time-weighted smoothing correction. When the time-weighted coefficient is less than 1, it can lead to a loss of resolution and potential residual artifacts.

Denoising. When the noise in acquired images is notable, it can adversely affect subsequent 3D reconstruction, leading to artifacts. To address this, we developed light-field denoising (LF-denoising[37]), a self-supervised transformer framework leveraging spatial–angular redundancy on the basis of the high-dimensional light-field measurements to achieve high-fidelity denoising without relying on temporal information and avoiding associated artifacts in the spatial domain. By treating multiple spatial–angular images as a collective whole, LF-denoising effectively suppresses noise without oversmoothing, thereby preserving high spatial resolution. However, the process still relied on manual determination of whether denoising was necessary. To address this, we incorporated an automated module into the pipeline, as detailed in Supplementary Fig. 11. The central angular view is used to calculate the single-image SNR (Methods). If the SNR exceeds 15 dB, the image is considered to require no denoising, whereas, if the SNR is less than 15 dB, the raw spatial–angular images are input into LF-denoising for reducing noise. The threshold is empirically determined. The code for LF-denoising can be obtained from GitHub (https://github.com/LF-denoising/LF-denoising). During network training, we used simulated beads, bubbles, tubes and scanning volumes of sliced samples as the dataset and trained for 50 epochs, taking 8 h on an NVIDIA A100 GPU. For inference, the spatial–angular data of each sub-FOV was divided into 25 patches, each with a size of 81 × 128 × 128 (view × height × width) for separate processing. The overlap region between adjacent patches contained 16 × 16 (height × width) pixels. Lastly, image stitching within each sub-FOV was performed on the basis of sigmoid fusion[61].

Aberration correction. Although optical design minimizes aberrations as much as possible, manufacturing errors and alignment eccentricities may still introduce slight, spatially nonuniform aberrations that remain in the optical system. Aberrations are difficult to remove in traditional 2D imaging[31]. To further correct system aberrations in RUSH3D-HR, wDAO[3] is used to estimate spatially nonuniform aberrations through wave-optics modeling and generate corresponding PSFs for use in the subsequent 3D reconstruction process. By calculating the disparity distances between images from different angles, wDAO can dynamically correct the wavefronts across the entire FOV in postprocessing with the measurement of high-resolution light-field information, which estimates and compensates for the wavefront aberrations for every local region without reducing the data acquisition speed. In previous studies[3], the full FOV was divided into 12 sub-FOVs for aberration estimation. In this work, we further subdivided the full FOV into 35 sub-FOVs as described above, resulting in an individual area of approximately 400 × 400 μm^2, within which the aberrations can be considered relatively consistent, allowing wDAO to more finely correct spatially nonuniform aberrations. Note that a smaller sub-FOV can theoretically provide a more precise correction of spatially varying aberrations. However, because the marginal utility of finer partitioning is limited, the resulting enhancement in image quality would be minimal compared to the substantial escalation in computational cost. Therefore, dividing the entire FOV into 35 sub-FOVs is standardized throughout the pipeline.

Parallel AI reconstruction and volume stitching. Because of the ultralarge volume of RUSH3D-HR data, each frame has a size of 14,000 × 10,000 × 100 voxels after reconstruction, nearing 20 GB. To address this, we used the previously developed SeReNet[34] to accelerate the 3D reconstruction process. SeReNet is a physics-driven self-supervised network designed for the 3D reconstruction of light-field microscopy data, achieving near-diffraction-limited resolution with millisecond-level processing speeds. Its design is intended to

eliminate the dependency on data-driven supervised training mechanisms, thereby facilitating robust performance across diverse biological samples. The code for SeReNet can be obtained from GitHub (https://github.com/kimchange/SeReNet). On a single NVIDIA A100 GPU, the reconstruction of single-frame data takes 139 s. To further speed up the process, we used eight GPUs in parallel, implementing parallelized SeReNet and reducing the reconstruction time for one frame to 20 s. During network training, we used simulated beads, bubbles, tubes and scanning volumes of sliced samples as the dataset and trained for 800 epochs, taking 30 h on an NVIDIA A100 GPU. Lastly, all patches were stitched together across the entire FOV using sigmoid fusion[61] to generate a mesoscale, high-resolution 3D volume.

Fluorescent bead imaging and resolution characterization

To characterize the system resolution, we made a mixture of 1 µl of 1% 0.2-µm fluorescence beads (Thermo Scientific, TetraSpeck microspheres, T7280) and 1 ml of 1% agarose. The mixture was then placed in a glass-bottom dish (NEST Scientific, 801001), in which the 0.2-µm fluorescence beads were randomly distributed in the agarose and experimentally captured by RUSH3D-HR. For resolution evaluation, we quantified the resolution by measuring the FWHMs of their intensity profiles along lateral and axial dimensions. The FWHM values are presented as the mean ± s.d., which serve directly as the experimentally measured resolution values. Quantitative analysis showed that the resolution remained nearly consistent across the entire FOV, after wDAO correction for spatially nonuniform aberrations. While the resolution varied slightly at different axial planes, it remained uniform within an extended DOF of approximately 40 µm.

Animals

All biological experiments were performed with the ethical approval from the Animal Care and Use Committee of Tsinghua University (protocol 17-DQH1.G25-1) in accordance with institutional and national guidelines.

Intravital imaging in a skin injury model

Male WT C57BL/6J mice (7–8 weeks old) were housed under a 12-h light–dark cycle at 24 °C ambient temperature and 50% humidity with ad libitum access to food and water. For neutrophil and vascular labeling, mice received an intravenous (i.v.) injection of a 60-µl antibody mixture containing Alexa Fluor 488-conjugated anti-Ly-6G antibody (BioLegend, 127626) and Alexa Fluor 647-conjugated anti-CD31 antibody (BioLegend, 102416), each at 10% dilution in sterile PBS (Gibco, C10010500BT). After 2 h for antibody distribution, mice were anesthetized with Avertin (350 mg kg^{-1}, intraperitoneally (i.p.)). The dorsal skin was prepared by hair removal and disinfection with 75% (v/v) ethanol. A standardized 4-mm excision wound was created in the mid-dorsal region to exceed the imaging FOV, with an additional deep wound about 800 µm in diameter penetrating the dermis at one end.

For imaging, anesthetized mice were positioned in a customized chamber while maintaining physiological conditions using a thermoregulator (37 °C, ThermoStar System, RWD), with the wound apposed to a no. 1.5 coverslip. Physiological monitoring included isoflurane anesthesia (0.5% in O_2 at 0.75 L min^{-1}) and respiratory rate assessment. Time-lapse imaging was performed for 10 h using 488-nm and 640-nm laser excitation.

Intravital imaging in a liver failure model

Similar to skin imaging protocols, male C57BL/6J mice (7–8 weeks old) were used for intravital liver imaging. To induce hepatotoxicity, fasted mice received an i.p. injection of APAP (300 mg kg^{-1}; Cayman, 103-90-2). After 4 h, a 90-µl i.v. antibody cocktail containing Alexa Fluor 647-conjugated anti-Ly6G (BioLegend, 127610), Alexa Fluor 561-conjugated anti-F4/80 (Thermo Fisher, 505-4801-82) and wheat germ agglutinin (Thermo Fisher, W11261), each at 10% dilution in PBS (Gibco, C10010500BT), was premixed before injection for neutrophil, macrophage and vascular labeling.

Then, 20 min after injection, mice were anesthetized with Avertin (350 mg kg^{-1}, i.p.), and the liver was surgically exposed on a customized imaging holder fitted with a 170-µm coverslip. Intravital imaging was performed using RUSH3D-HR system with a thermoregulator (37 °C, ThermoStar Homeothermic System, RWD) under isoflurane anesthesia (0.5% in O_2 at 0.75 L min^{-1}). Multicolor imaging was achieved using sequential 488-nm, 555-nm and 640-nm laser excitation over 50 min.

Intravital imaging in an LPS-induced inflamed spleen model

Similar to liver imaging protocols, male C57BL/6J mice (7–8 weeks old) were used for intravital spleen imaging. LPS (*Escherichia coli* O111:B4, Sigma-Aldrich, L2630) was prepared as a 10 mg ml^{-1} solution in sterile PBS (Gibco, C10010500BT) and stored at 4 °C. Mice received an i.p. injection of LPS (5 mg kg^{-1}). Then, 30 min later, neutrophils were fluorescently labeled by i.v. injection of anti-Ly6G antibody (BioLegend, 127610) at 10% dilution in PBS through the tail vein.

After a 1-h recovery period, mice were anesthetized with Avertin (350 mg kg^{-1}, i.p.) and surgically prepared for imaging. The spleen was carefully exposed and immobilized on a customized holder with a 170-µm coverslip. Intravital imaging was performed using the RUSH3D-HR system with a thermoregulator (37 °C, ThermoStar System, RWD) under isoflurane anesthesia (0.5% in O_2 at 0.75 L min^{-1}). For data acquisition, continuous imaging was performed over 5 h with 640-nm laser excitation.

EA treatment

Before EA treatment, mice were acclimated to cylindrical restrainers for 30 min daily over three consecutive days to minimize restraint stress[62–64]. During treatment sessions, mice were placed in specialized holders that secured the trunk while allowing free movement of the head and limbs. All EA procedures were performed on conscious animals without anesthesia.

The treatment was administered using two pairs of sterile stainless-steel acupuncture needles (diameter: 0.16 mm) inserted bilaterally at the ST36 (Zusanli) acupoint[49]. This location was precisely identified as 4 mm distal to the knee joint and 2 mm lateral to the anterior tibial tubercle. Electrical stimulation was delivered using a Master-9 stimulator (AMPI) connected to two ISO-Flex isolators (AMPI), with parameters set as follows: frequency, 10 Hz; pulse width, 50 µs; alternating current, 0–0.5 mA. Each treatment session lasted 20 min. Following EA treatment, mice underwent intravital spleen imaging as described.

Mouse brain slice clearing, immunohistochemical staining and imaging

Male C57BL/6J mice (8–12 weeks old) were housed under a 12-h light–dark cycle with ad libitum access to food and water. Before all perfusion experiments, mice were deeply anesthetized with Avertin working solution (0.16 ml per 10 g, containing 19.2 mg ml^{-1} tribromoethanol) through intraperitoneal injection. The mice were perfused with ice-cold saline followed by ice-cold 4% (w/v) paraformaldehyde (PFA) in PBS. After immersing the brains in PFA for 4 h, they were vibration-sectioned into 1-mm-thick slices and rinsed with PBS for several times. The brain slices were made transparent according to the VIVIT[65] procedures. For immunohistochemical staining of neuronal cell nuclei, the brain slices were incubated with primary antibodies (1:500 to 1:2,000) in PBST (0.01 M PBS containing 0.4% Triton X-100) at room temperature with shaking for 1 day. The slices were subsequently washed three times in PBST for 10 min each time. We then incubated the slices with fluorescently conjugated secondary antibodies (1:800) in PBST at room temperature with shaking for 4 h. After washing with PBS three times for 10 min each time, the slices were incubated with 2 mg ml^{-1} disuccinimidyl glutarate dissolved in 0.01 M PBS for 2–4 h at room temperature to prevent antibody dissociation during tissue clearing.

FRC analysis

The FRC resolution[66] is defined as a metric to estimate the resolution of nonstandard biological images. Firstly, high-resolution volumetric images are reconstructed using a pipeline that incorporates self-supervised denoising for noise suppression and virtual-scanning-based motion correction for artifact reduction. Secondly, to ensure the accuracy of the FRC analysis, each image is spatially partitioned into four independent subsets, I_1, I_2, I_3 and I_4, which are then transformed into the frequency domain as F_1, F_2, F_3 and F_4. We meticulously inspected these Fourier spectra to confirm the absence of isolated high-frequency peaks, which are indicators of processing artifacts, thereby ensuring the reliability of the FRC analysis. Thirdly, the FRC is subsequently computed using the following formula:

$$FRC_1(r_i) = \frac{\sum_{r\in r_i} F_1(r)\cdot F_4(r)^*}{\sqrt{\sum_{r\in r_i} {F_1}^2(r)\cdot \sum_{r\in r_i} {F_4}^2(r)}},$$

$$\mathrm{FRC}_2(r_i) = \frac{\sum_{r\in r_i} F_2(r)\cdot F_3(r)^*}{\sqrt{\sum_{r\in r_i} {F_2}^2(r)\cdot \sum_{r\in r_i} {F_3}^2(r)}},$$

where r represents the spatial coordinates in the frequency domain and r_i is the ith frequency bin. We verified the profile of the resulting FRC curves to ensure a consistent downward trend, confirming that the correlation is driven by genuine structural information rather than correlated noise. The average of the cutoff frequencies at which $\mathrm{FRC}_1(r_i)$ and $\mathrm{FRC}_2(r_i)$ drop below the 1/7 threshold is taken as the image resolution.

Performance metrics

We used lateral SBP, OTF, Strehl ratio, r.m.s. wavefront, peak-to-valley (PV) ratio, peak SNR (PSNR), structural similarity index measure (SSIM), SBR and SNR to evaluate the performance of Kunlun and RUSH3D-HR. Specifically, following the foundational principles of Fourier optics[67], the lateral SBP represents the information capacity of an objective lens, defined as the product of the spatial extent and the spatial frequency bandwidth. This product effectively quantifies the total number of resolvable spots under the objective lens, which can be calculated as

$$\mathrm{SBP} = 4\cdot\frac{\pi(d_{\mathrm{FOV}}/2)^2}{(0.5\lambda/NA)^2}$$

(effective pixels) for one-photon imaging[3],

$$\mathrm{SBP} = 4\cdot\frac{\pi(d_{\mathrm{FOV}}/2)^2}{(0.46\lambda/NA^{0.91})^2}$$ (effective pixels) for multiphoton imaging[68], where λ is the wavelength of light and d_{FOV} is the diameter of FOV covered by the objective lens, which can be obtained directly from the manufacturers or derived by

$$d_{\mathrm{FOV}} = \frac{\mathrm{FN}}{M},$$

where FN and M denote the field number and magnification of objective lens, respectively.

The OTF is defined as a performance metric that measures the degradation of contrast in the image compared to contrast in the object, which can be calculated as

$$\mathrm{OTF} = \frac{I_{\max} - I_{\min}}{I_{\max} + I_{\min}},$$

where $I_{\max}$ and $I_{\min}$ denote the maximum intensity to the white bars and minimum intensity to the black bars of a bar target at a specific frequency, respectively.

The Strehl ratio is defined as a measure of the quality of optical image formation, which can be calculated as the ratio of the peak intensity of the actual PSF to the peak intensity of the ideal PSF without aberration, described as

$$\text{Strehl ratio} = \frac{I_{\mathrm{actual}}(0)}{I_{\mathrm{ideal}}(0)},$$

where $\text{Strehl ratio} = \frac{I_{\mathrm{actual}}(0)}{I_{\mathrm{ideal}}(0)}$, is the peak light intensity at the focal point of an actual optical system and $I_{\mathrm{actual}}(0)$ is the peak light intensity of an ideal diffraction-limited system, exemplified by the central intensity of an Airy disk.

The r.m.s. wavefront describes the average deviation of the optical aberration from the ideal image plane, which can be calculated as

$$\text{r.m.s.} = \sqrt{\frac{1}{A}\int_A (W-\overline{W})^2\,dA},$$

where A is the image plane, W is the wavefront at the image plane and $\overline{W} = \frac{1}{A}\int_A W\cdot dA$ is the mean wavefront deviation.

The PV ratio is defined as a ratio of signal height in peak apex and signal height in the end of peak, which can be calculated as

$$PV = W_{\max} - W_{\min},$$

where $W_{\max}$ and $W_{\min}$ denote the maximum value and minimum value of the wavefront, respectively.

The PSNR is defined as a metric to evaluate the quality of a reconstructed or compressed signal compared to a reference signal, which can be represented as

$$\mathrm{PSNR} = 10\log_{10}\frac{max(\|X\|_2^2)}{\|X-Y\|_2^2}.$$

The SSIM is defined as a perceptual metric that quantifies the similarity between two images by considering changes in structural information, luminance and contrast, which can be calculated as

$$\mathrm{SSIM} = \frac{\left(2\mu_X\mu_Y + (0.01\cdot\max(X))^2\right)(2\sigma_{XY} + (0.03\cdot\max(X))^2)}{\left(\mu_X^2+\mu_Y^2 + (0.01\cdot\max(X))^2\right)(\sigma_X^2+\sigma_Y^2 + (0.03\cdot\max(X))^2)},$$

where μ_X and μ_Y are the averages of X and Y, σ_X and σ_Y denote the corresponding s.d. and σ_{XY} is the corresponding cross-covariance. We firstly obtained the local SSIM maps using sliding 2D Gaussian windows (11 × 11, s.d. = 1.5) for 2D images; then, the average of these local maps was returned as the final SSIM value.

The SBR is defined as the ratio of the signal intensity to the background intensity, which can be calculated as

$$\mathrm{SBR} = 10\cdot\log_{10}\frac{\max(X)}{\mu_x},$$

where μ_X is the average of X. We firstly obtained the local SBR maps using sliding 2D Gaussian windows (200 × 200 pixels, s.d. = 30 pixels) for 2D images; then, the average of these local maps was returned as the final SBR value.

The SNR is defined as a measure of signal strength relative to background noise. We used a single-image SNR estimation method[69] to calculate the SNR of images without the corresponding clean images as reference, which can be represented as

$$\mathrm{SNR} = \frac{\Phi^{\mathrm{NF}}(0,0) - \mu^2}{\Phi(0,0) - \Phi^{\mathrm{NF}}(0,0)},$$

where $\Phi(0,0)$ is the value of autocorrelation function (ACF) of the image at 2D offset $(0,0)$, μ is the average of the image and $\Phi^{NF}(0,0)$ is the value

of ACF of the noise-free image at zero offset, which can be estimated with the average of $\Phi(0,1)$ and $\Phi(0,-1)$.

Data analysis

The data acquisition was accomplished using our customized image acquisition software. All data processing and analysis were accomplished with customized Python (version 3.8.20) and MATLAB (MathWorks, MATLAB 2019a) scripts. The 3D rendering was performed by Imaris (version 9.0.1) with 'volume' modules. The 3D tracking of neutrophils in living mouse dorsal skins and spleens was carried out using Imaris (version 9.0.1) with the 'cell tracking' function. The 3D cell pose segmentation of neutrophils in mouse skins was carried out using the Cellpose[70] algorithm. For migrasome event detection in living mouse livers, we detected all contours on neutrophil channel each frame and filtered contours with diameter < 3 µm, which is approximately the maximum diameter of a migrasome[71]. The circularity of each contour was calculated using $\frac{4\pi A}{C^2}$, where A represents the size of the contour and C represents the circumference of the contour. The contours with circularity < 0.4 were filtered out. To exclude contours caused by noise, we further calculated the local intensity range by subtracting from the local minimum intensity from center intensity and the local intensity range less than half of the whole frame intensity range was filtered out. Lastly, the contours that appeared at least twice in the following three frames were considered as migrasome contours. Once a migrasome contour was detected, its center intensity and intensity at the same location on previous frame were recorded. In the following frames, the position deviation of this contour was recorded for speed calculation.

Reporting summary

Further information on research design is available in the Nature Portfolio Reporting Summary linked to this article.

Data availability

The published article contains all data generated during this study. The raw imaging data are available on Zenodo (https://doi.org/10.5281/zenodo.20701541)[72]. Source data are provided with this paper.

Code availability

The codes generated during this study with example data are available from GitHub (https://github.com/RUSH3D-HR/RUSH3D-HR) and Zenodo (https://doi.org/10.5281/zenodo.20715408)[73].

References

60. Marr, D. & Hildreth, E. Theory of edge detection. *Proc. R. Soc. Lond. B Biol. Sci.* **207**, 187–217 (1980).
61. Luo, X., Zhang, Z. & Wu, X. Image fusion using region segmentation and sigmoid function. In *Proc. 22nd International Conference on Pattern Recognition* (ed O'Conner, L.) https://doi.org/10.1109/ICPR.2014.190 (IEEE, 2014).
62. Shen, S. Y. et al. The neuroprotective effects of GPR55 against hippocampal neuroinflammation and impaired adult neurogenesis in CSDS mice. *Neurobiol. Dis.* **169**, 105743 (2022).
63. Ma, X. et al. Spinal neuronal GRK2 contributes to preventive effect by electroacupuncture on cisplatin-induced peripheral neuropathy in mice. *Anesth. Analg.* **134**, 204–215 (2022).
64. Chen, Y. et al. Neuronal GRK2 regulates microglial activation and contributes to electroacupuncture analgesia on inflammatory pain in mice. *Biol. Res.* **55**, 5 (2022).
65. Gao, Y. et al. VIVIT: resolving trans-scale volumetric biological architectures via ionic glassy tissue. *Cell* **188**, 6079–6095 (2025).
66. Koho, S. et al. Fourier ring correlation simplifies image restoration in fluorescence microscopy. *Nat. Commun.* **10**, 3103 (2019).
67. Lohmann, A. W., Dorsch, R. G., Mendlovic, D., Zalevsky, Z. & Ferreira, C. Space–bandwidth product of optical signals and systems. *J. Opt. Soc. Am. A* **13**, 470–473 (1996).
68. Zipfel, W. R., Williams, R. M. & Webb, W. W. Nonlinear magic: multiphoton microscopy in the biosciences. *Nat. Biotechnol.* **21**, 1369–1377 (2003).
69. Thong, J. T. L., Sim, K. S. & Phang, J. C. H. Single-image signal-to-noise ratio estimation. *Scanning* **23**, 328–336 (2001).
70. Stringer, C., Wang, T., Michaelos, M. & Pachitariu, M. Cellpose: a generalist algorithm for cellular segmentation. *Nat. Methods* **18**, 100–106 (2021).
71. Zhao, X. et al. Identification of markers for migrasome detection. *Cell Discov.* **5**, 27 (2019).
72. Chen, W. Imaging data for RUSH3D-HR. *Zenodo* https://doi.org/10.5281/zenodo.20701541 (2026).
73. Chen, W. RUSH3D-HR/RUSH3D-HR: v1.zenodo. *Zenodo* https://doi.org/10.5281/zenodo.20715408 (2026).

Acknowledgements

We thank H. Ma, Y. Si, X. Chen and Y. Chen for their assistance in preparing mouse experiments and H. Zhou for the discussion of data analysis.

Author contributions

Conceptualization, Q.D., W.W. and J.W. Methodology, Z.L., J.W., W.C., M.J. and L.Z. Biological experiments, M.W., W.C., Z.L. and Q.Z. Investigation, Z.L. and M.W. Visualization, Z.L., W.C., T.W., Y.Y. and C.Z. Funding acquisition, Q.D., W.W., J.W., Z.L. and M.W. Project administration, Q.D., W.W. and J.W. Supervision, Q.D., W.W. and J.W. Writing—original draft, Z.L., M.W., W.C., J.W., W.W. and Q.D. Writing—review and editing, Z.L., M.W., W.C., J.W., W.W. and Q.D.

Funding

This work was supported by the Natural Science Foundation of China (62525506, 62088102, 62575154 and 82441061), Beijing Natural Science Foundation (Z240011, 4254114 and JR25021), New Cornerstone Science Foundation through the XPLORER PRIZE, Fundamental and Interdisciplinary Disciplines Breakthrough Plan of the Ministry of Education of China (JYB2025XDXM504) and Beijing Key Laboratory of Cognitive Intelligence.

Competing interests

Q.D., J.W. and Y.Y. are founders and equity holders of Zhejiang Hehu Technology. Y.Y. and C.Z. are employees of Zhejiang Hehu Technology. The other authors declare no competing interests.

Additional information

Supplementary information The online version contains supplementary material available at https://doi.org/10.1038/s41587-026-03231-z.

Correspondence and requests for materials should be addressed to Jiamin Wu, Wei Wang or Qionghai Dai.

Peer review information *Nature Biotechnology* thanks Bernd Rieger, Weijian Yang and the other, anonymous, reviewer(s) for their contribution to the peer review of this work.

Reprints and permissions information is available at www.nature.com/reprints.

nature portfolio

Corresponding author(s): Jiamin Wu, Wei Wang, Qionghai Dai

Last updated by author(s): Jun 17, 2026

Reporting Summary

Nature Portfolio wishes to improve the reproducibility of the work that we publish. This form provides structure for consistency and transparency in reporting. For further information on Nature Portfolio policies, see our Editorial Policies and the Editorial Policy Checklist.

Statistics

For all statistical analyses, confirm that the following items are present in the figure legend, table legend, main text, or Methods section.

n/a	Confirmed
☐	☒ The exact sample size (*n*) for each experimental group/condition, given as a discrete number and unit of measurement
☐	☒ A statement on whether measurements were taken from distinct samples or whether the same sample was measured repeatedly
☐	☒ The statistical test(s) used AND whether they are one- or two-sided *Only common tests should be described solely by name; describe more complex techniques in the Methods section.*
☒	☐ A description of all covariates tested
☐	☒ A description of any assumptions or corrections, such as tests of normality and adjustment for multiple comparisons
☐	☒ A full description of the statistical parameters including central tendency (e.g. means) or other basic estimates (e.g. regression coefficient) AND variation (e.g. standard deviation) or associated estimates of uncertainty (e.g. confidence intervals)
☐	☒ For null hypothesis testing, the test statistic (e.g. *F*, *t*, *r*) with confidence intervals, effect sizes, degrees of freedom and *P* value noted *Give P values as exact values whenever suitable.*
☒	☐ For Bayesian analysis, information on the choice of priors and Markov chain Monte Carlo settings
☒	☐ For hierarchical and complex designs, identification of the appropriate level for tests and full reporting of outcomes
☐	☒ Estimates of effect sizes (e.g. Cohen's *d*, Pearson's *r*), indicating how they were calculated

Our web collection on statistics for biologists contains articles on many of the points above.

Software and code

Policy information about availability of computer code

Data collection	The data acquisition was accomplished using our customized image acquisition software.
Data analysis	The data acquisition was accomplished using our customized image acquisition software. All data processing and analysis were accomplished with customized Python (3.8.20 version) and MATLAB (MathWorks, MATLAB 2019a) scripts. The 3D rendering was performed by Imaris (Imaris 9.0.1 software) with Volume modules. The 3D tracking of neutrophils in living mouse dorsal skins and spleens was carried out using Imaris (Imaris 9.0.1 software) cell tracking function. The 3D cell pose segmentation of neutrophils in mouse skins was carried out using Cellpose algorithm. For migrasome event detection in living mouse livers, we detected all contours on neutrophil channel each frame and filtered contours with diameter less than 3 μm, which is approximately the maximum diameter of a migrasome. The circularity of each contour was calculated using $4\pi A/C^2$, where A represents the size of the contour and C represents the circumference of the contour. The contours with circularity less than 0.4 were filtered out. To exclude contours caused by noise, we further calculated the local intensity range by subtracting from local minimum intensity from center intensity, and the local intensity range less than half of the whole frame intensity range was filtered out. Finally, the contours that appeared at least twice in the following 3 frames were considered as migrasome contours. Once a migrasome contour was detected, its center intensity and intensity at the same location on previous frame were recorded. In the following frames, the position deviation of this contour was recorded for speed calculation.

For manuscripts utilizing custom algorithms or software that are central to the research but not yet described in published literature, software must be made available to editors and reviewers. We strongly encourage code deposition in a community repository (e.g. GitHub). See the Nature Portfolio guidelines for submitting code & software for further information.

Data

Policy information about availability of data

All manuscripts must include a data availability statement. This statement should provide the following information, where applicable:

- Accession codes, unique identifiers, or web links for publicly available datasets
- A description of any restrictions on data availability
- For clinical datasets or third party data, please ensure that the statement adheres to our policy

The published article contains all data generated during this study and the raw imaging data is available on Zenodo (https://doi.org/10.5281/zenodo.20701541)

Research involving human participants, their data, or biological material

Policy information about studies with human participants or human data. See also policy information about sex, gender (identity/presentation), and sexual orientation and race, ethnicity and racism.

Reporting on sex and gender	No human research participants in this study
Reporting on race, ethnicity, or other socially relevant groupings	Not involved in this study
Population characteristics	Not involved in this study
Recruitment	Not involved in this study
Ethics oversight	Not involved in this study

Note that full information on the approval of the study protocol must also be provided in the manuscript.

Field-specific reporting

Please select the one below that is the best fit for your research. If you are not sure, read the appropriate sections before making your selection.

☒ Life sciences ☐ Behavioural & social sciences ☐ Ecological, evolutionary & environmental sciences

For a reference copy of the document with all sections, see nature.com/documents/nr-reporting-summary-flat.pdf

Life sciences study design

All studies must disclose on these points even when the disclosure is negative.

Sample size	The sample size (n) of each experiment is provided in the figure/table legends in the main manuscript and supplementary information files. In order to conduct statistical significance tests, all sample sizes (n) were set to be greater than 3.
Data exclusions	No data were excluded for the analysis.
Replication	Data shown in Figs. 3-6 are representative of n = 3 experiments. Characterization data shown in Fig. 2 and Supplementary Figs. 4-6, 9-16 are representative of n = 6 experiments. Supplementary Fig. 17 is representative of n = 3 experiments.
Randomization	Randomization was not relevant to this study, since no experimental group was formed.
Blinding	Blinding was not relevant to this study, since no group allocation was performed.

Reporting for specific materials, systems and methods

We require information from authors about some types of materials, experimental systems and methods used in many studies. Here, indicate whether each material, system or method listed is relevant to your study. If you are not sure if a list item applies to your research, read the appropriate section before selecting a response.

Materials & experimental systems

n/a	Involved in the study
☐	☒ Antibodies
☒	☐ Eukaryotic cell lines
☒	☐ Palaeontology and archaeology
☐	☒ Animals and other organisms
☒	☐ Clinical data
☒	☐ Dual use research of concern
☒	☐ Plants

Methods

n/a	Involved in the study
☒	☐ ChIP-seq
☒	☐ Flow cytometry
☒	☐ MRI-based neuroimaging

Antibodies

Antibodies used	Ly6G antibody (Biolegend, #127610), Ly6G antibody (BioLegend, #127626), F4/80 (Thermo Fisher, #505-4801-82), CD31 antibody (BioLegend, #102416).
Validation	All monoclonal antibodies were validated from the Biolegend website (https://www.biolegend.com, cats# 127610, cats# 127626, cats#102416) and Thermo Fisher website (https://www.thermofisher.cn, cats# 505-4801-82), and purchased to perform mouse experiments.

Animals and other research organisms

Policy information about studies involving animals; ARRIVE guidelines recommended for reporting animal research, and Sex and Gender in Research

Laboratory animals	Mice (C57BL6/J, ~7-8 weeks).
Wild animals	Not involved in this study.
Reporting on sex	The mice used in this project are male.
Field-collected samples	Not involved in this study.
Ethics oversight	Animal protocol procedures were reviewed and approved by the Institutional Animal Care and Use Committee office of Tsinghua University.

Note that full information on the approval of the study protocol must also be provided in the manuscript.

Plants

Seed stocks	Not involved in this study.
Novel plant genotypes	Not involved in this study.
Authentication	Not involved in this study.